ESA CONTRACT REPORT

Contract Report to the European Space Agency

Tech Note - Phase II - WP1100
SMOS Monitoring Report
Number 2: Nov 2010 - Nov 2011

Joaquín Muñoz Sabater,
Mohamed Dahoui,
Patricia de Rosnay,
Lars Isaksen

ESA/ESRIN Contract
400010703/10/NL/FF/fk

European Centre for Medium-Range Weather Forecasts
Europäisches Zentrum für mittelfristige Wettervorhersage
Centre européen pour les prévisions météorologiques à moyen terme

ECMWF

Series: ECMWF ESA Project Report Series

A full list of ECMWF Publications can be found on our web site under:
http://www.ecmwf.int/publications/

Contact: library@ecmwf.int

European Centre for Medium Range Weather Forecasts
Shinfield Park, Reading, RG2 9AX, England

Contract Report to the European Space Agency

Tech Note - Phase II - WP1100
SMOS Monitoring Report
Number 2: Nov 2010 - Nov 2011

Authors: Joaquín Muñoz Sabater,
Mohamed Dahoui,
Patricia de Rosnay,
Lars Isaksen

Technical Note - Phase-II - WP1100
Monitoring Report Number 2: Nov 2010 - Nov 2011
ESA/ESRIN Contract 4000101703/10/NL/FF/fk

European Centre for Medium-Range Weather Forecasts
Shinfield Park, Reading, Berkshire, UK

December 2011

	Name	Company
First version prepared by (November 2011)	J. Muñoz Sabater	ECMWF
Quality Visa	E. Källén	ECMWF
Application Authorized by		ESA/ESTEC

Distribution list:

ESA/ESRIN
Luc Govaert
Susanne Mecklenburg
Steven Delwart
ESA ESRIN Documentation Desk

SERCO
Raffaele Crapolicchio

ESA/ESTEC
Tania Casal
Matthias Drusch
Klaus Scipal

ECMWF
HR
Division & Section Heads

Contents

Abstract

Contracted by the European Space Agency (ESA), the European Centre for Medium-Range Weather Forecasts (ECMWF) is involved in global monitoring and data assimilation of the Soil Moisture and Ocean Salinity (SMOS) mission data. For the first time, a new innovative remote sensing technique based on radiometric aperture synthesis is used in SMOS to observe soil moisture over continental surfaces and ocean salinity over oceans. Monitoring SMOS data (i.e. the comparison between the observed value and the model equivalent of that observation) is therefore of special interest and a requirement prior to assimilation experiments. This report is the second Monitoring Report delivered to ESA. The objective is to report on the monitoring activities of SMOS data over land and sea on a long term basis, investigating also the multi-angular and multi-polarised aspect of the SMOS observations. This report presents results for one year (November 2010- November 2011) of SMOS data monitoring in Near Real Time obtained through the SMOS monitoring suite at ECMWF.

1 Introduction

ECMWF has developed an operational chain which monitors SMOS data in Near Real Time (NRT) at global scale, as explained in (Sabater et al. 2010). Monitoring is carried out routinely for each new type of satellite data brought into the operational Integrated Forecasting System (IFS) at ECMWF. In Numerical Weather Prediction systems monitoring is mainly focused on the comparison between the observed variable and the model equivalent simulating that observation, because this is the quantity used in the analysis.
For SMOS, monitoring is produced separately for land and oceans. The reason is the strong contrast between the dielectric constant of water bodies and land surfaces, which in turn produces very different emissivities and observed brightness temperatures at the top of the atmosphere. Thus, monitoring SMOS data separately over land and oceans increases the sensitivity to the statistical variables. Moreover, the multi-angular and multi-polarised aspect of the observations is also accounted for in the monitoring chain by monitoring the data independently for several incidence angles of the observations and for two polarisation states at the antenna reference frame.
The developed framework makes it possible to obtain daily statistics of the observations, the model equivalent of the observations computed by the Community Microwave Emission Model (CMEM) [(Drusch et al. 2009; de Rosnay et al. 2009a)], and the difference between the two quantities, the so called first-guess departures. The statistics are computed over several weeks of data. This is a very robust way to identify systematic differences between modelled values and observations. Furthermore it also set the basis to investigate and understand the new observations before they become active in the ECMWF land assimilation scheme.

This Monitoring Report (MR2) on SMOS data is the second monitoring report delivered to ESA. In the first one [(Sabater et al. 2011b)] the monitoring website and statistical products were described. This monitoring report shows results obtained since November 2010, the date when the monitoring suite started to produce routinely statistics in Near Real Time (NRT) at ECMWF.

2 SMOS observations at ECMWF

SMOS NRT products are processed at the European Space Astronomy Centre (ESAC) in Madrid (Spain) and sent to ECMWF via the SMOS Data Processing Ground Segment (DPGS) interface. The product used at ECMWF is the NRT product which are geographically sorted swath-based maps of brightness temperatures. The geolocated product received at ECMWF is arranged in an equal area grid system called ISEA 4H9 (Icosahedron Snyder Equal Area grid with Aperture 4 at resolution 9) [see (Matos and Gutierrez 2004)]. For this grid, the centre of the cell grids are at equal distance of 15 km over land, with a standard deviation of 0.9 km. For the NRT product, the resolution is coarser over oceans as they present lower heterogeneities that continental surfaces. The format of the NRT product is the Binary Universal Form for the Representation of meteorological data (BUFR). Each message in BUFR format corresponds to a snapshot where the integration time is 1.2 seconds. In average, each snapshot contains around 4800 subsets over land.

3 Monitoring over land

In this section some of the more relevant results obtained with the monitoring suite [see a description in part III of (Sabater et al. 2010) and (Sabater et al. 2011b)] over land surfaces are shown.

3.1 Simulations of brightness temperatures

In order to simulate brightness temperatures at L-band and compare them to the SMOS observations, ECMWF has developed the Community Microwave Emission Model (CMEM) (de Rosnay et al. 2009b). It constitutes the forward model operator for low frequency passive microwave brightness temperatures of the surface. Although for SMOS purposes it is used at 1.4 GHz, potentially it can be used up to 20 GHz. This software package is fully coded in Fortran-90 language. It has been designed to be highly modular providing a good range of I/O interfaces for the Numerical Weather Prediction Community. CMEM surface forcing comes from the integration of the operational H-TESSEL (Hydrology Tiled ECMWF Scheme for Surface Exchanges over Land) land surface scheme [(Balsamo et al. 2009)]. H-TESSEL is forced with meteorological fields of surface pressure, specific humidity, air temperature and wind speed at the lowest atmospheric level. The surface radiation and precipitation flux represent 3 hourly averages, and they are kept constant over a 3 hour period. The integration of HTESSEL provides the soil moisture and soil temperature fields, as well as snow depth and snow density fields, which are then coupled with CMEM to simulate ECMWF first-guess L-band brightness temperatures. Additional land surface information needed is soil texture data obtained from the Food and Agriculture Organization (FAO) data set, whereas sand and clay fractions have been computed from a lookup table according to (Salgado 1999). The soil roughness standard deviation of height (σ) parameter in CMEM is set to 2.2 cm as in (Holmes et al. 2008). Vegetation type is derived from the H-TESSEL classification, whereas a MODIS climatology is used to derive leaf area index (LAI).
CMEM's physics is based on the parameterisations used in the L-Band Microwave Emission of the Biosphere [LMEB, (Wigneron et al. 2007)] and Land Surface Microwave Emission Model [LSMEM, (Drusch et al. 2001)]. The modular architecture of CMEM makes it possible to consider different parameterisations of the soil dielectric constant, the effective temperature, the roughness effect of the soil and the vegetation and atmospheric contribution opacity models. In the current configuration of CMEM, the vegetation opacity model of (Kirdyashev et al. 1979) is used, in combination with the (Wang and Schmugge 1980) dielectric model, the (Wigneron et al. 2001) effective temperature model and the simple soil roughness model of (Choudhury et al. 1979). The atmospheric contribution is accounted for as in (Pellarin et al. 2003). This combination of parameterisations were shown to be well suited for brightness temperature modelling (Drusch et al. 2009; de Rosnay et al. 2009a; Sabater et al. 2011a). However these results are based on local and regional scale experiments and a global sensitivity study with SMOS data has not yet been undertaken.
Note also that CMEM is a SMOS Validation and Retrieval Teams (SVRT) tool freely available at *http://www.ecmwf.int/research/ESA_projects/SMOS/cmem/cmem_index.html*. More information about CMEM can be found in (de Rosnay et al. 2009b).

3.2 Time-averaged geographical mean fields.

Fig. 1 and Fig. 2 show the brightness temperatures as a function of the incidence angle for August 2011 and for several incidence angles, averaged in boxes of 0.25 degrees. Fig. 1 is for XX polarisation whereas Fig. 2 is for YY polarisation. Both figures show large values of brightness temperatures as it corresponds to the summer season at the North Hemisphere. Both polarisations behave as theoretically expected, i.e., brightness temperatures decreasing with the incidence angle for XX polarisation (from the averaged 240 K at 10 degrees to 219 K at 60 degrees) and increasing for YY polarisation (from the averaged 242 K at 10 degrees to 260 at 60 degrees). Hard Radio Frequency Interference (RFI) is filtered out by rejecting brightness temperatures greater than 350 K or lower than 50 K. However, a substantial RFI is still present in many parts of Europe and Asia, and this is the reason why in all figures observations close to 350 K are found.

Fig. 3 shows the evolution of the SMOS observed brightness temperatures standard deviation at global scale, from November 2010 to August 2011 (one averaged value per month), at 40 degrees incidence angle and for XX polarisation. Fig. 4 is the equivalent figure for YY polarisation. These statistics are also computed in spatial boxes of 0.25 degrees. RFI affected areas are clearly observed in these plots, in red colour. For these areas, this means that, on average over a month, the observations have a variability larger than 40 K. In most of the cases this is not the result of a natural large variability of the observations, but rather caused by external sources contaminating the L-band. Many of these sources of RFI are intermittent and they can contaminate large areas around the source. They are especially strong in China and North of India, but also significant contamination is found around the Middle East and the East of Europe. It is observed that the YY polarisation is in general more affected by RFI in regards to the extension of the affected area, mainly the North of China, however India is less affected in YY polarisation. January 2010 looks specially bad, but during this month the NRT data was degraded due to a stability test of the SMOS instrument and the variability of the observations was negatively affected. An improvement is observed from November 2010 to August 2011. The improvement is especially significant in Europe and India. From May 2011 both polarisations in Western Europe are quite clean of intermittent sources of RFI. Areas showing large variability during a month, and not contaminated by RFI, are very important for assimilation experiments, as there potentially are good sources of information about soil moisture.

Figs. 5 and 6 show the evolution of the first-guess departures (observed brightness temperatures minus the CMEM model equivalents) at the antenna reference frame from November 2010 to August 2011 (one averaged value per month), at 40 degrees incidence angle and for XX and YY polarisations, respectively. The emission over snow and ice covered areas is not currently well represented by CMEM. This is specially significant at the XX polarisation for which simulated brightness temperatures are strongly underestimated. Therefore, for this polarisation a strong correlation can be observed between snow covered areas (and areas with strong orography) and the first-guess departures during the winter months in the North Hemisphere. For example, the Pyrinees, the Alps and the Himalayas can be clearly distinguished in Fig. 5g. This effect is also present in the YY polarisation, but is much weaker. For YY polarisation, a systematic negative bias is present, which it may be linked to the current lack of variability of the roughness parameterisation of CMEM. Areas strongly affected by RFI are also clearly visible in Fig. 6, as an apparently strong overestimation of the observed brightness temperatures is seen. These results are, however, very dependent on the incidence angle. For example, for YY polarisation the bias are very close to zero for the largest incidence angles.

In Fig. 7 a zoom over Europe is presented for YY polarisation. This figure shows small red dots, many of them stable and fixed in time, where very large disagreement between the observations and the model are found. These dots display fixed sources of RFI. For example, although the situation in Spain has clearly being improved in the last year, there are still a few sources remaining, clearly in Madrid, Zaragoza and Barcelona.

Luckily, these dots in Europe show sources of limited intensity and the contaminated area is mainly constrained to the location of the source.

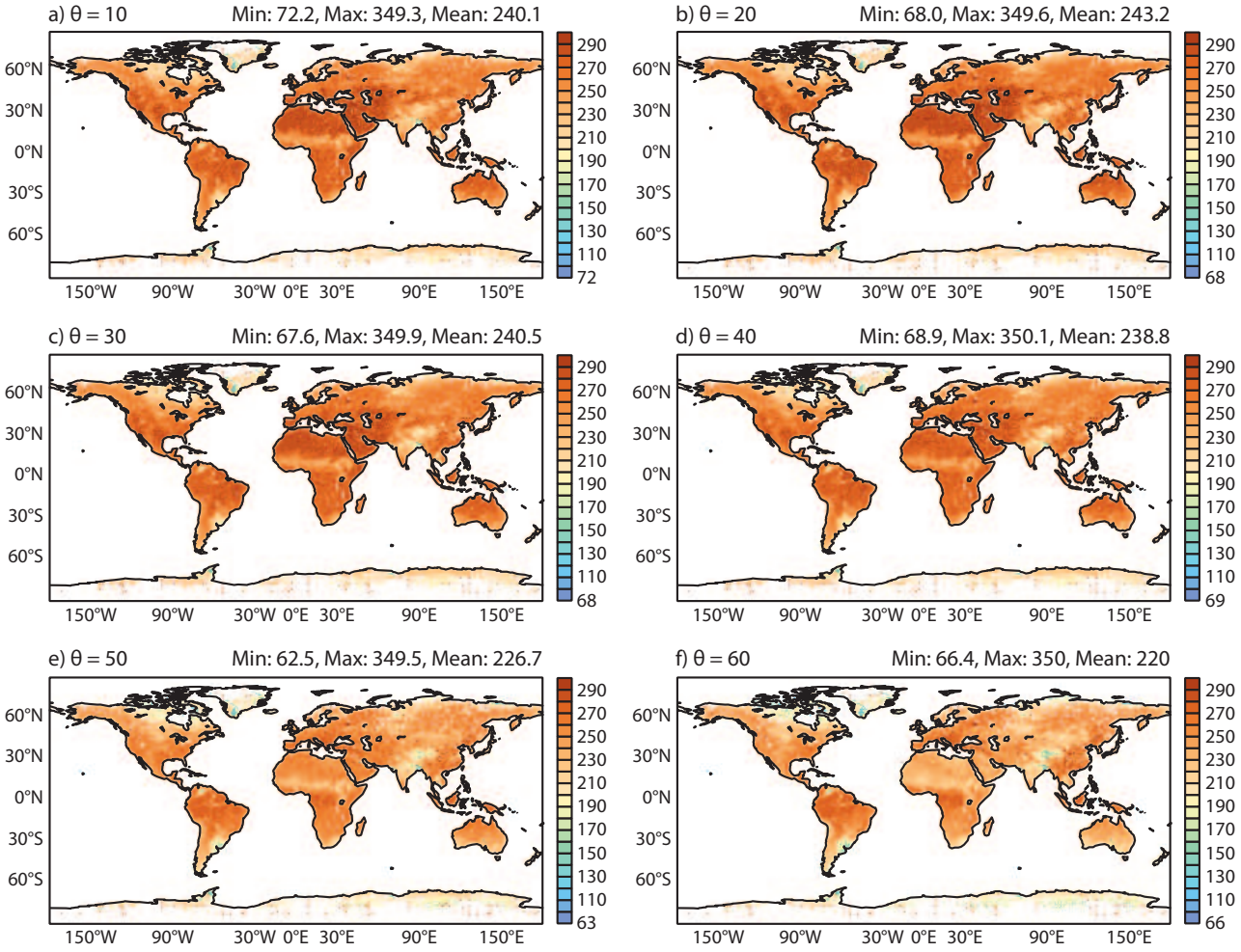

Figure 1: August 2011, geographical mean of the SMOS observed brightness temperatures as a function of the incidence angle, for XX polarisation. Each value represents a mean value of all the data inside a box of 0.25 degrees.

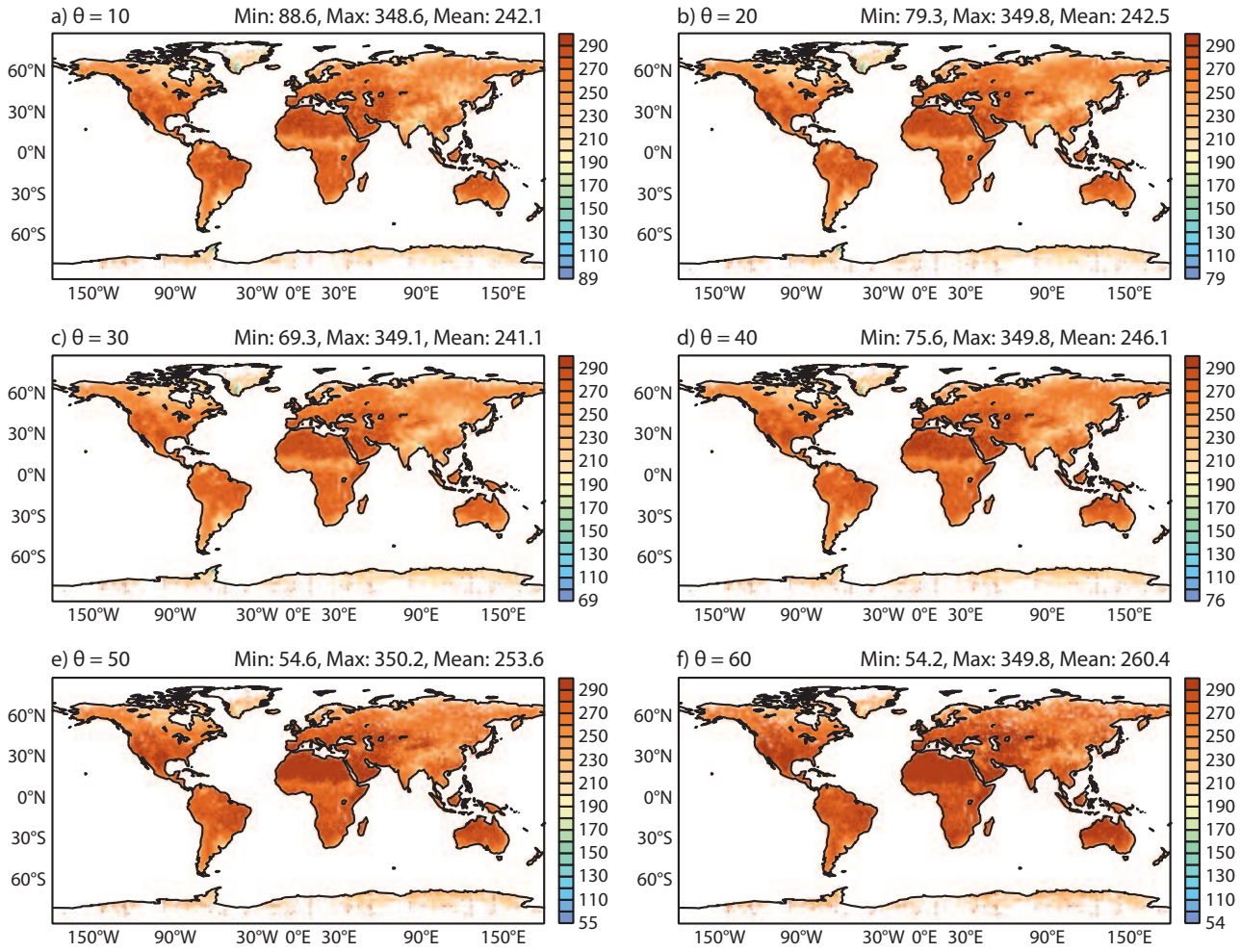

Figure 2: As in Fig. 1 but for YY polarisation.

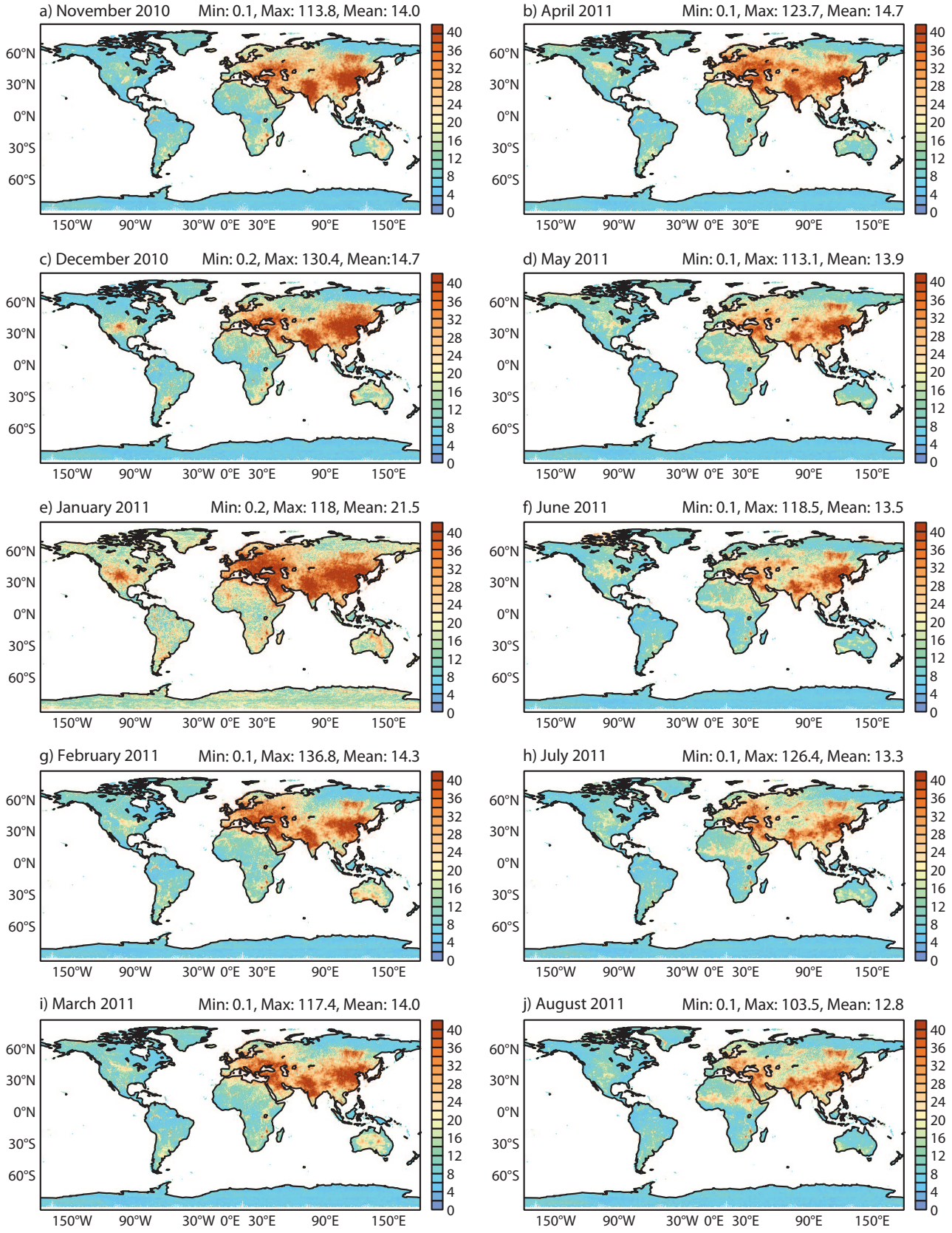

Figure 3: Monthly global mean of the SMOS observed brightness temperatures standard deviation, for XX polarisation, from November 2010 to August 2011. Each value represents a mean value of all the data inside a box of 0.25 degrees. The incidence angle is 40 degrees.

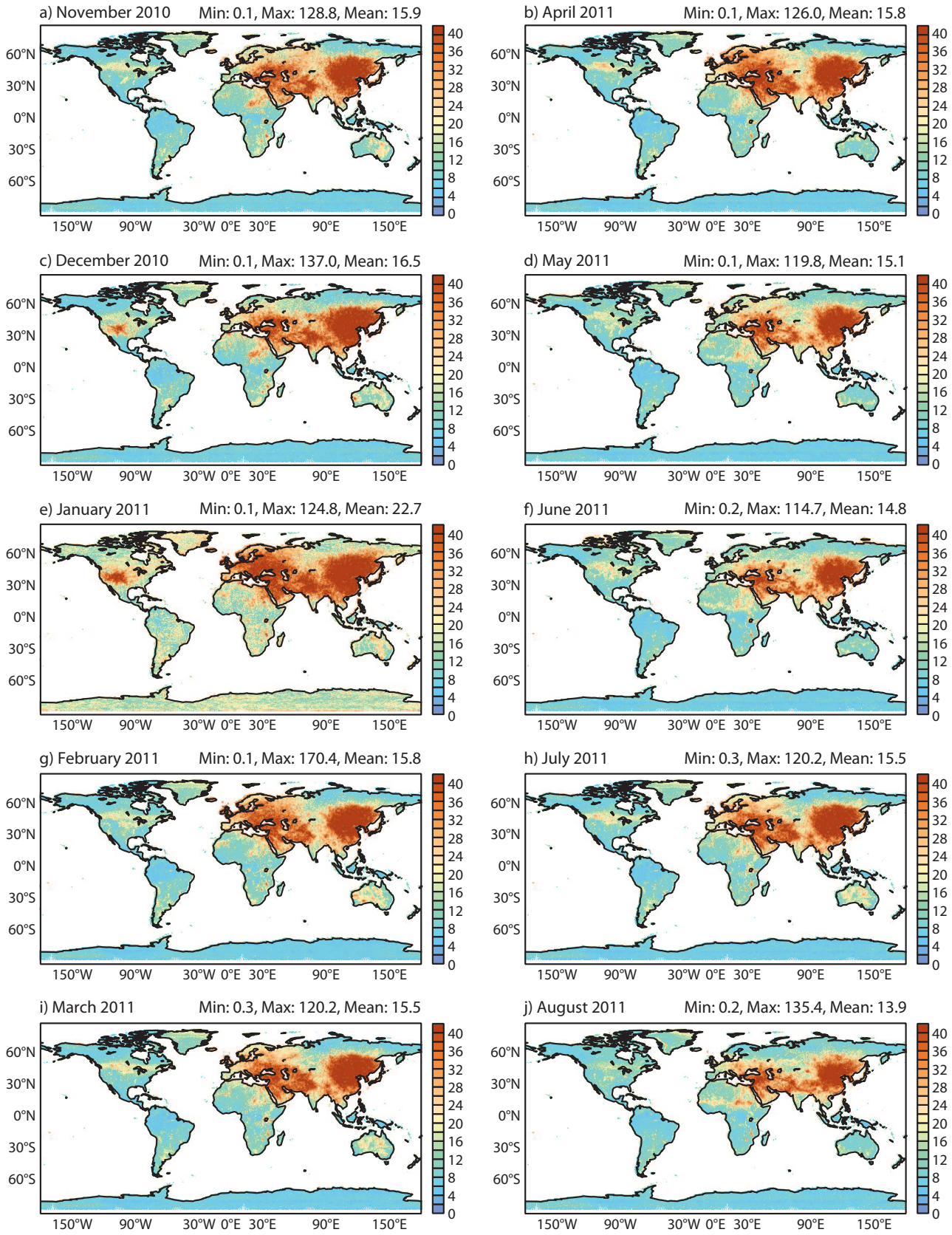

Figure 4: As Fig. 3, but for YY polarisation.

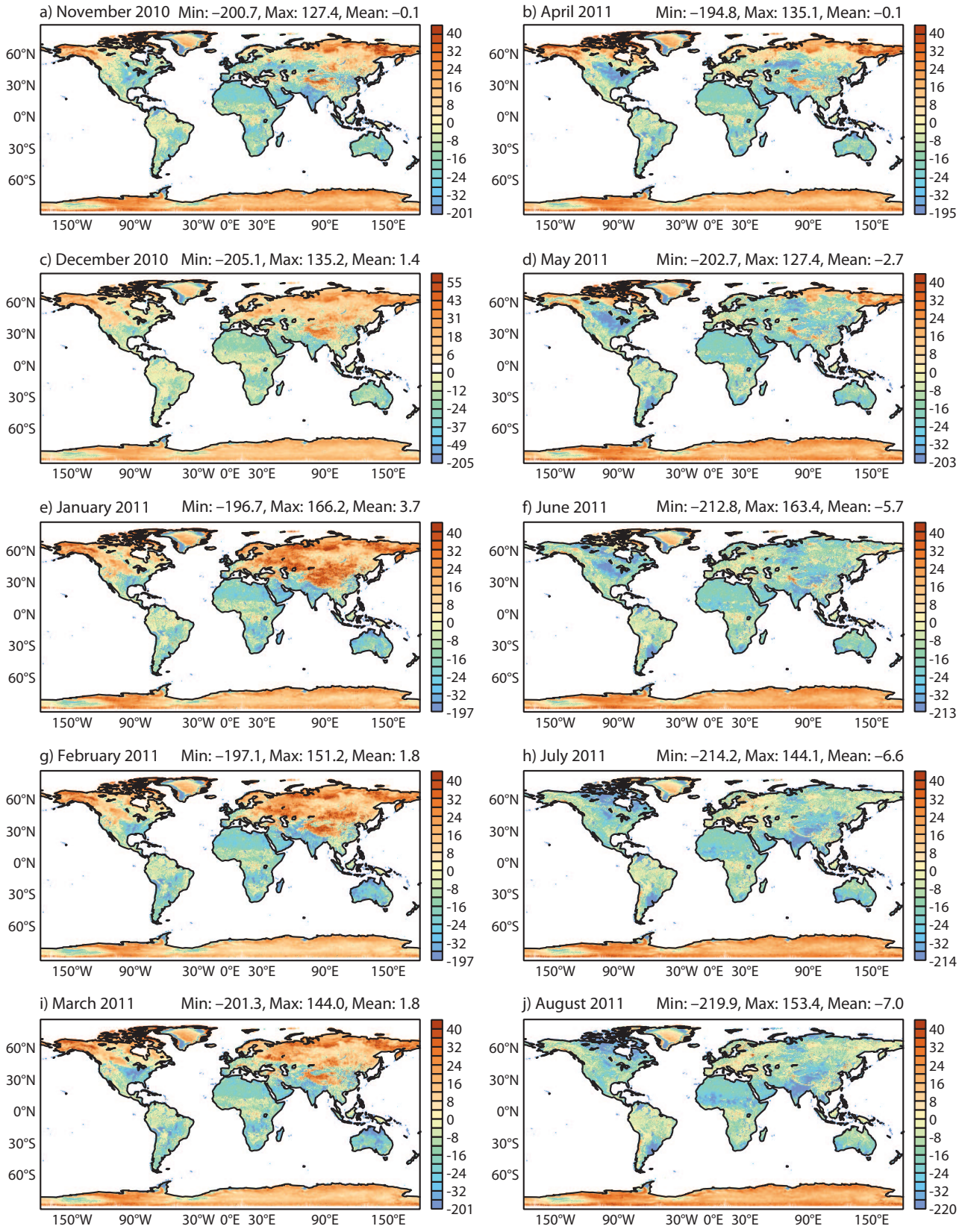

Figure 5: Monthly global mean of the first-guess departures between SMOS observed brightness temperatures and the CMEM model equivalents, for XX polarisation at 40 degrees incidence angle.

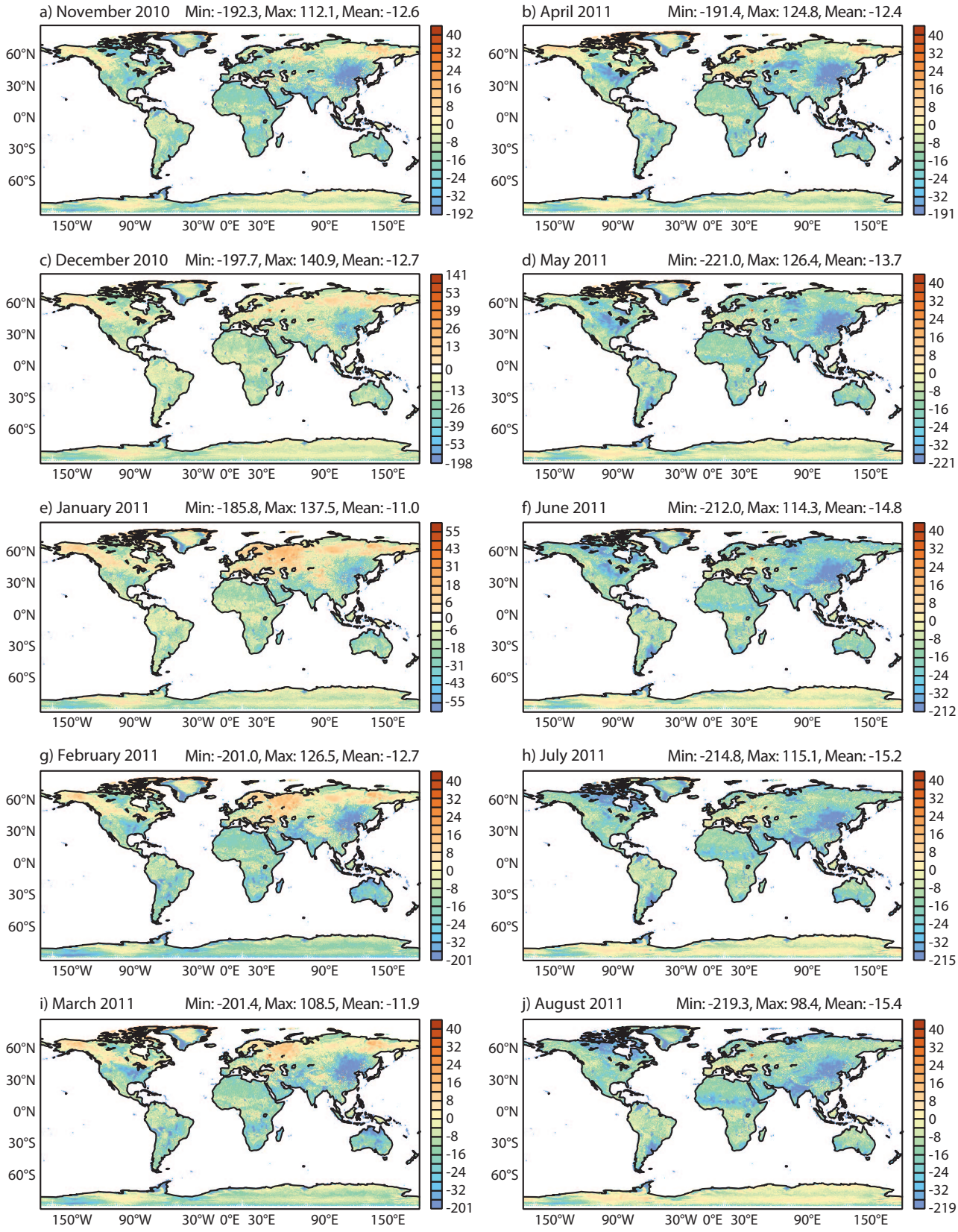

Figure 6: As in Fig. 5, but for YY polarisation.

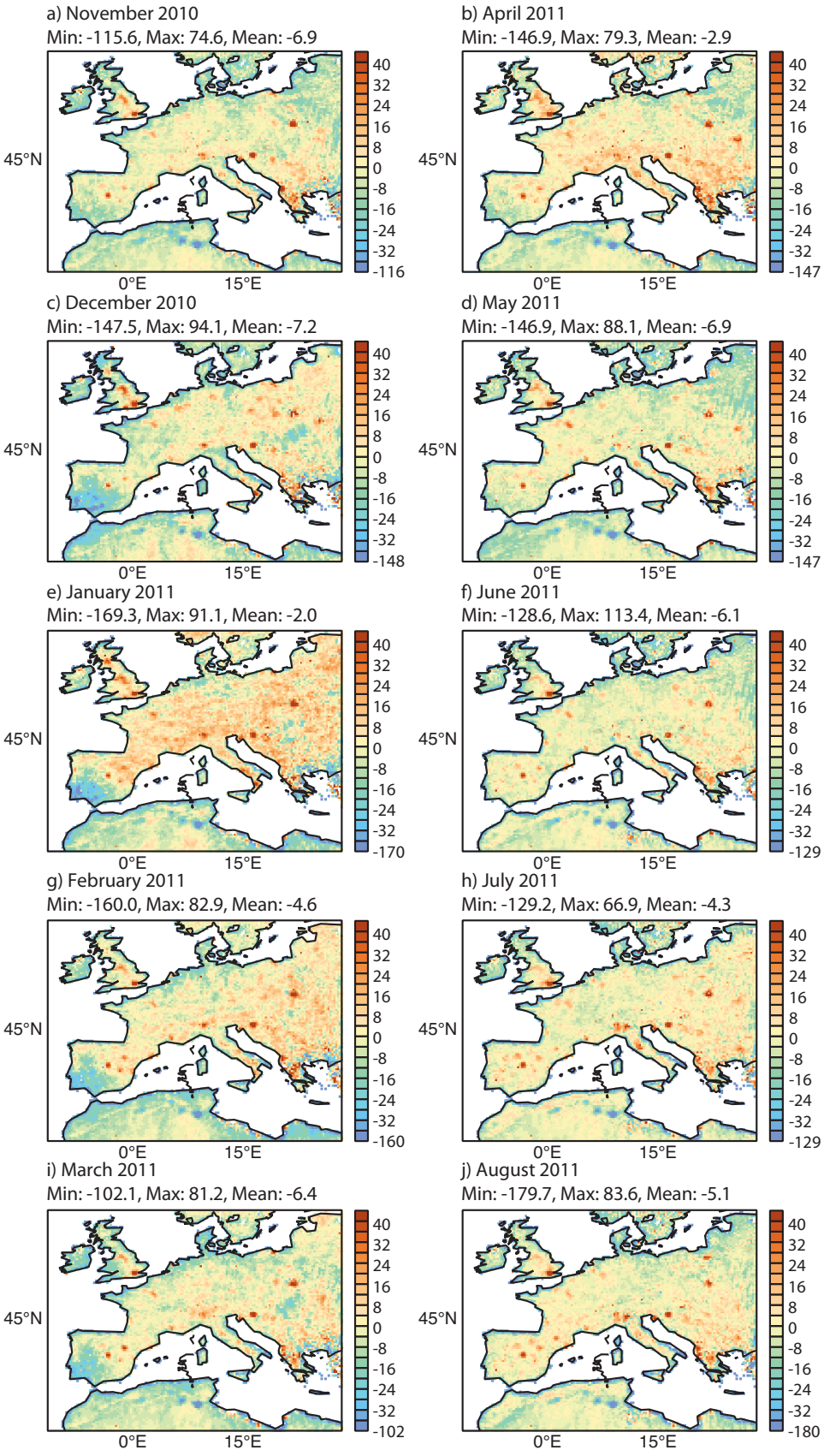

Figure 7: As in Fig. 6, but zoom in over Europe.

3.3 Time series

Figs. 8 to 15 present time series of the observed brightness temperatures, CMEM model equivalents, first guess departures and number of observations, from November 2010 to August 2011. Each value represents one mean value per ECMWF 4DVAR 12 hours assimilation cycle averaged at global scale, hemisphere or continent.

Fig. 8 presents the results obtained at global scale over land pixels. Left panel is for XX polarisation and right panel for YY polarisation. For YY polarisation an almost systematic negative bias is observed the whole year, increasing between April and May around 4 K in absolute value. During this period most of the melting of the snow takes place, which explains this difference. This effect is stronger for XX polarisation because our model is more sensitive over snow for this polarisation, as seen in Fig. 5. A slightly larger variability of the bias is also observed on the YY polarisation. A possible explanation is the larger influence of RFI on the YY polarisation, as seen in Fig. 4, but also a larger variability is observed during the snow months at the North Hemisphere for XX polarisation.

At the end of December 2010 a stability test of the SMOS platform took place during 6 days, no data was produced during this period and this can clearly be seen in all the time series. During the following 2 weeks the science data was degraded and this explains the abnormal peaks at the beginning of January 2011. In addition, the NRT processor did not work as normal until 18 February 2011 and during this period the observed brightness temperatures were a few degrees larger, producing larger bias, as it can be observed for January 2011 in Figs. 3 and 4.

The standard deviation of the bias are smaller and more stable in the Southern Hemisphere (Fig. 10) than in the Northern Hemisphere (Fig. 9) due to the stronger presence of RFI in the Northern Hemisphere, and this is especially visible in the more affected YY polarisation. Especially strong values and variability is found in Europe (Fig. 11) and Asia (fig. 12) where values as large as 45 K and differences of 20 K between two consecutive cycles are found. South America (Fig. 14) and Australia (Fig. 15) show more stable and lower values of the standard deviation of the bias, between 18 and 20 K for South America and slightly larger for Australia. The larger variability on the number of observations per Australia depends logically on the position of the satellite at the time of the acquisition.

In general, when compared to the observations the model underestimates the observed brightness temperatures during months with snow and overestimates them during the snow free months. Likewise, the observations show stronger sensibility over periods with snow than periods without snow, and the bias are more stable from mid-May onwards. The low presence of snow in the Southern Hemisphere explains why the bias are more stable throughout the whole year, although a systematic negative bias is found in South America and Australia. It is important to note that although for SMOS snow covered areas are interesting for monitoring purposes, observations over snow will not be used for assimilation experiments.

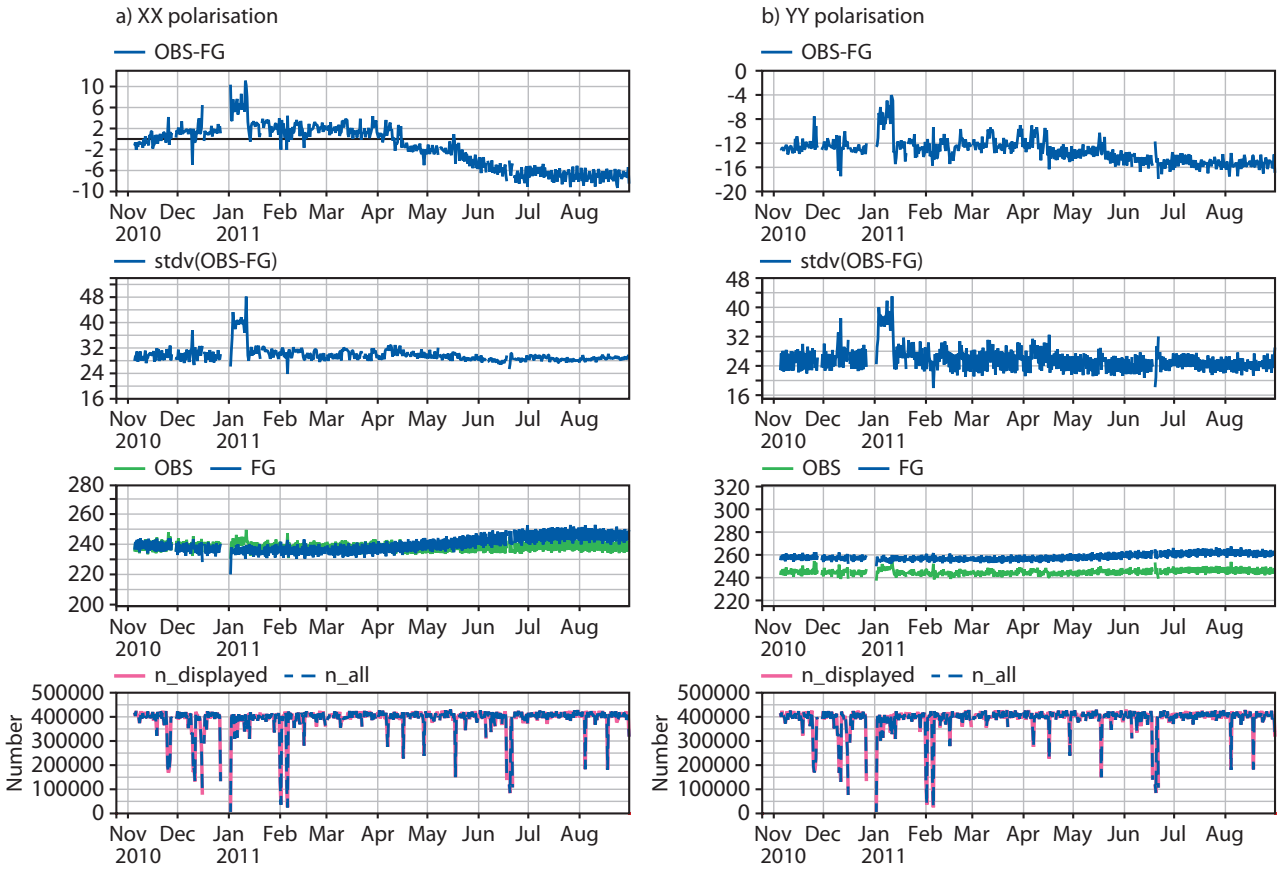

Figure 8: Global scale, time series from November 2010 to August 2011 over continental surfaces, at 40 degrees incidence angle, of mean bias (top figures), mean standard deviation of bias (second top row), comparison between observed brightness temperatures and the CMEM modeled equivalents (third row), and number of observations (bottom figures). Each value is an averaged value per ECMWF 4DVAR 12h cycle. Left panel is for XX polarisation, right panel for YY polarisation.

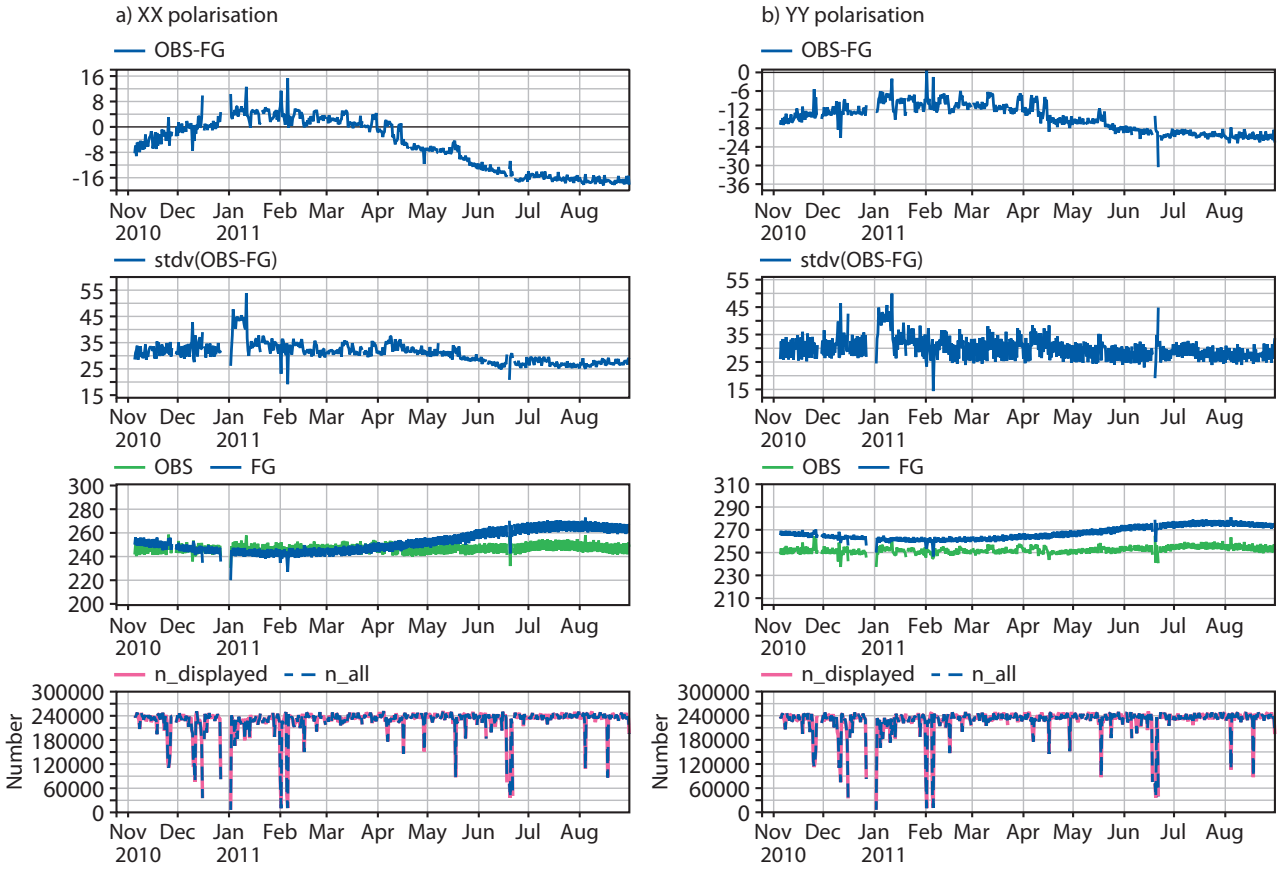

Figure 9: As in Fig. 8 but for the North Hemisphere.

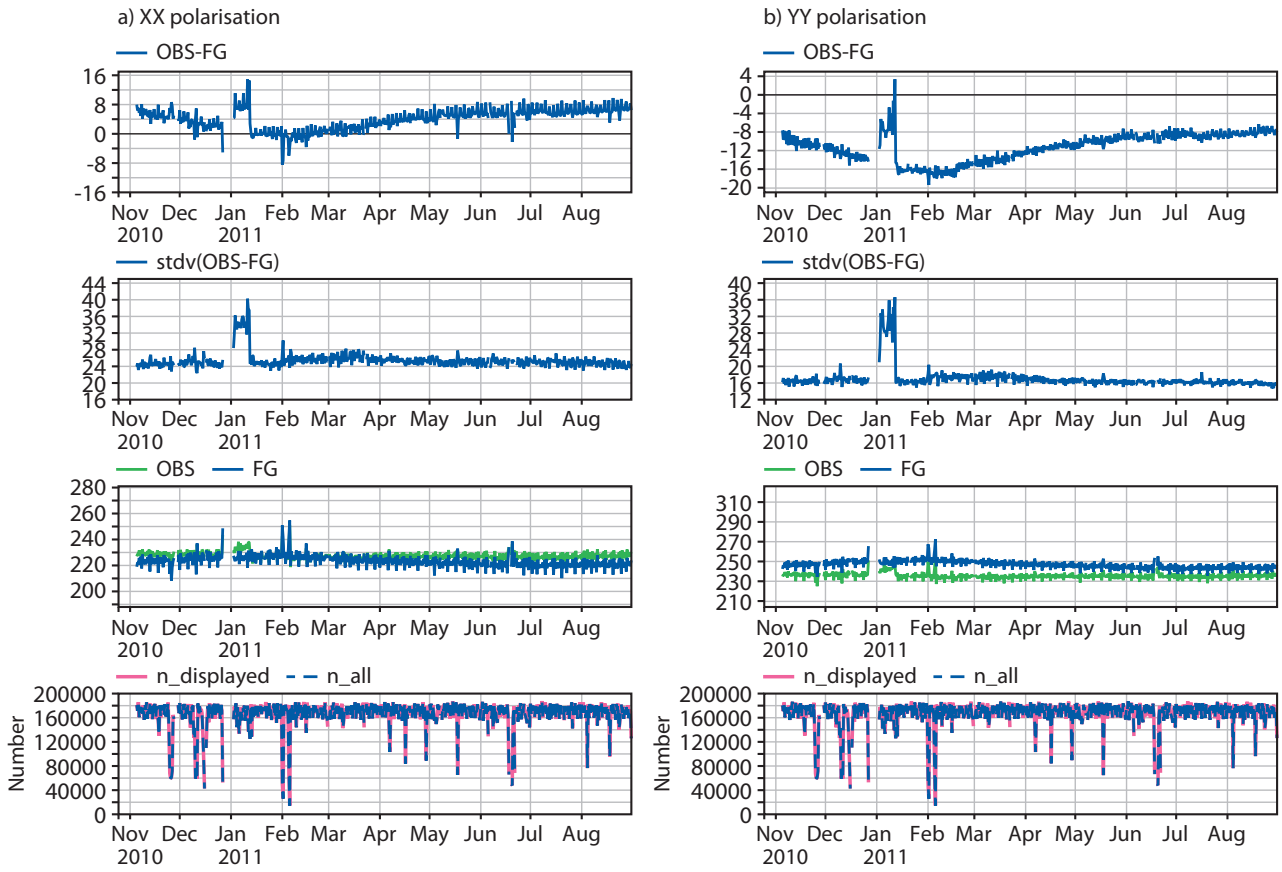

Figure 10: As in Fig. 8 but for the South Hemisphere.

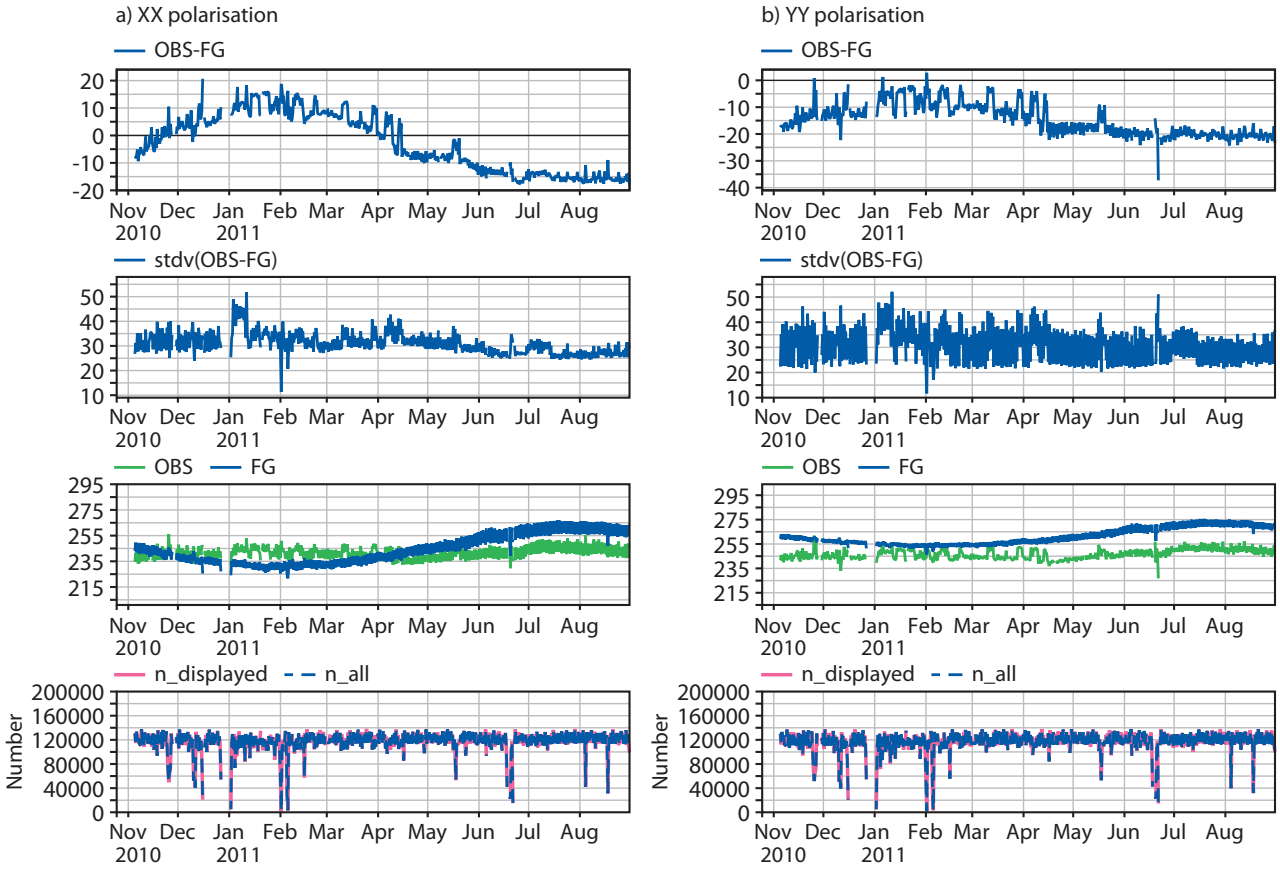

Figure 11: As in Fig. 8 but for Europe.

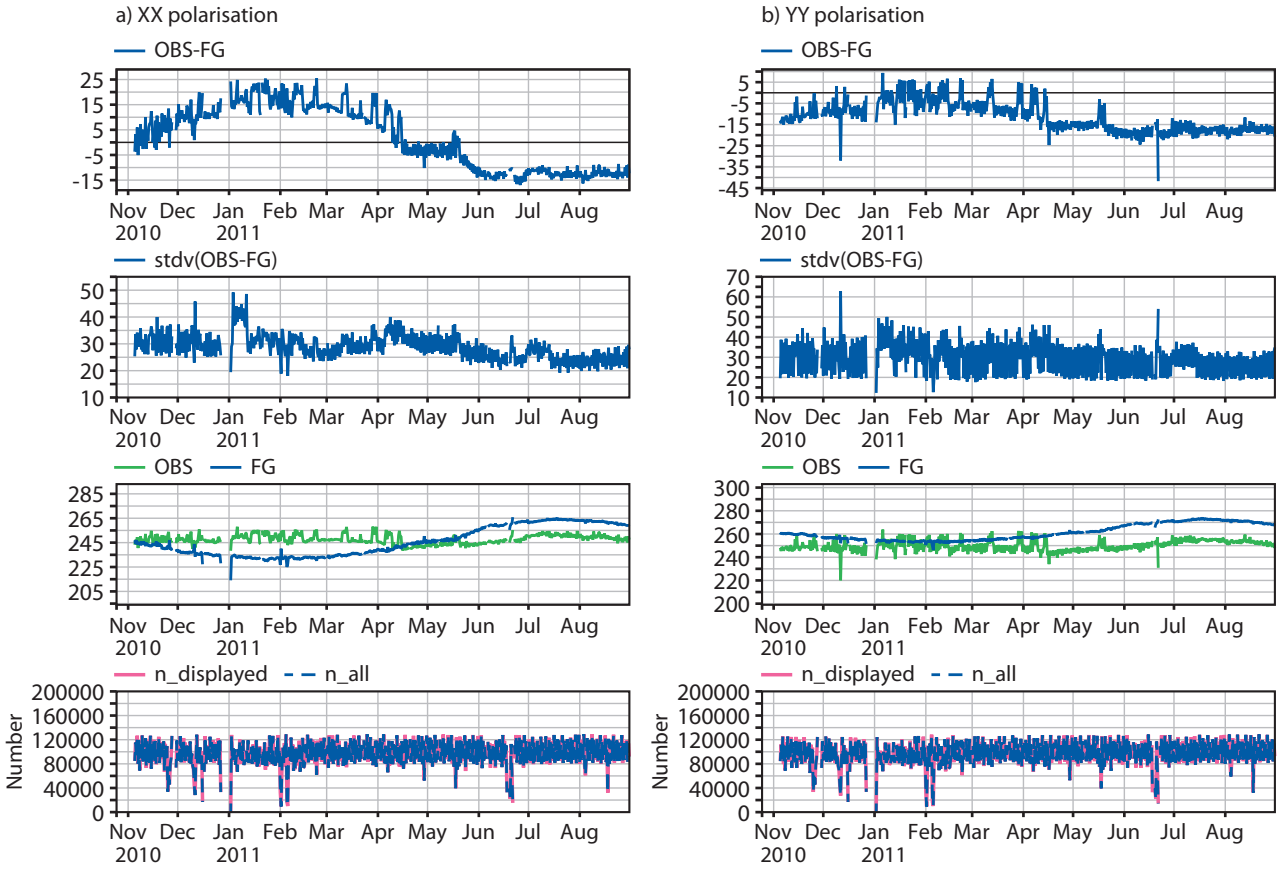

Figure 12: As in Fig. 8 but for Asia.

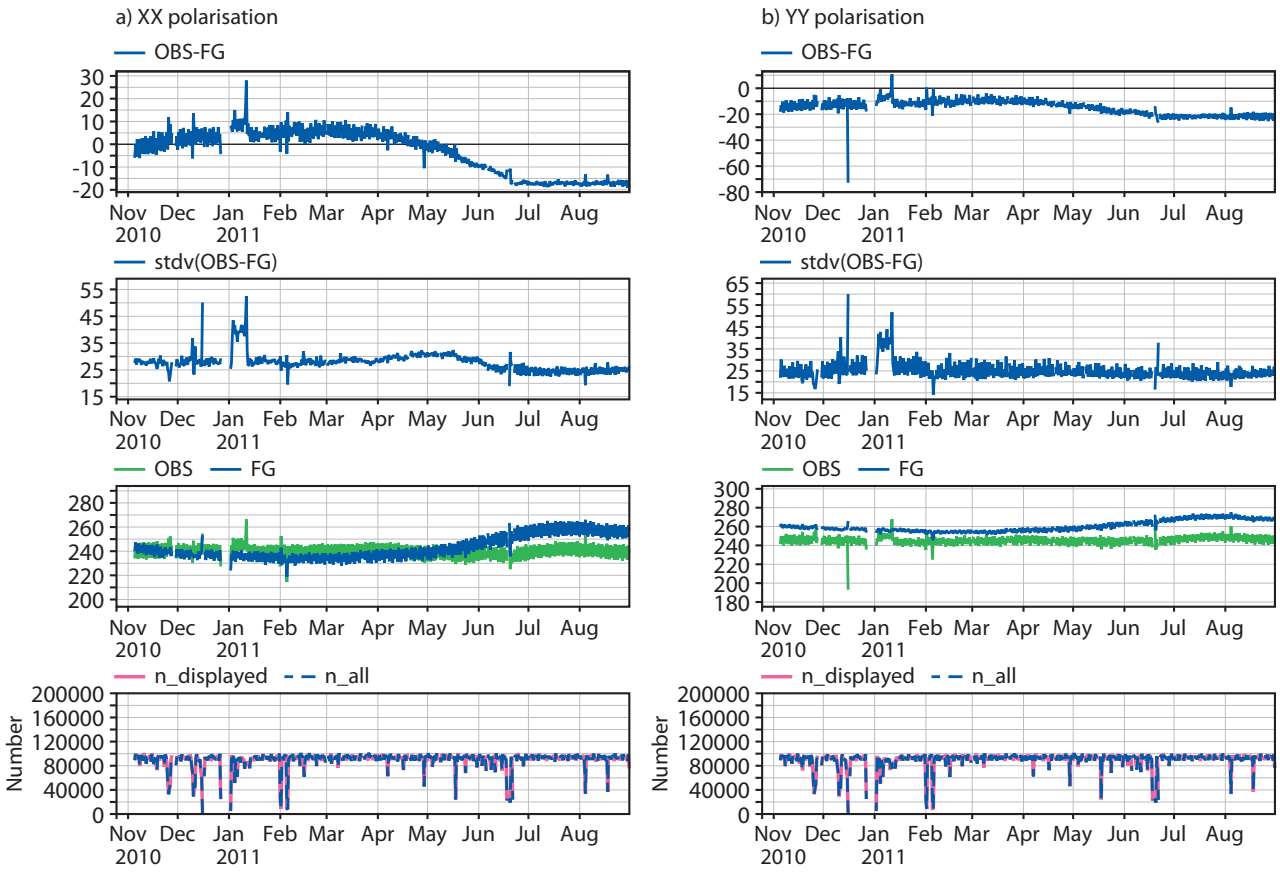

Figure 13: As in Fig. 8 but for North America.

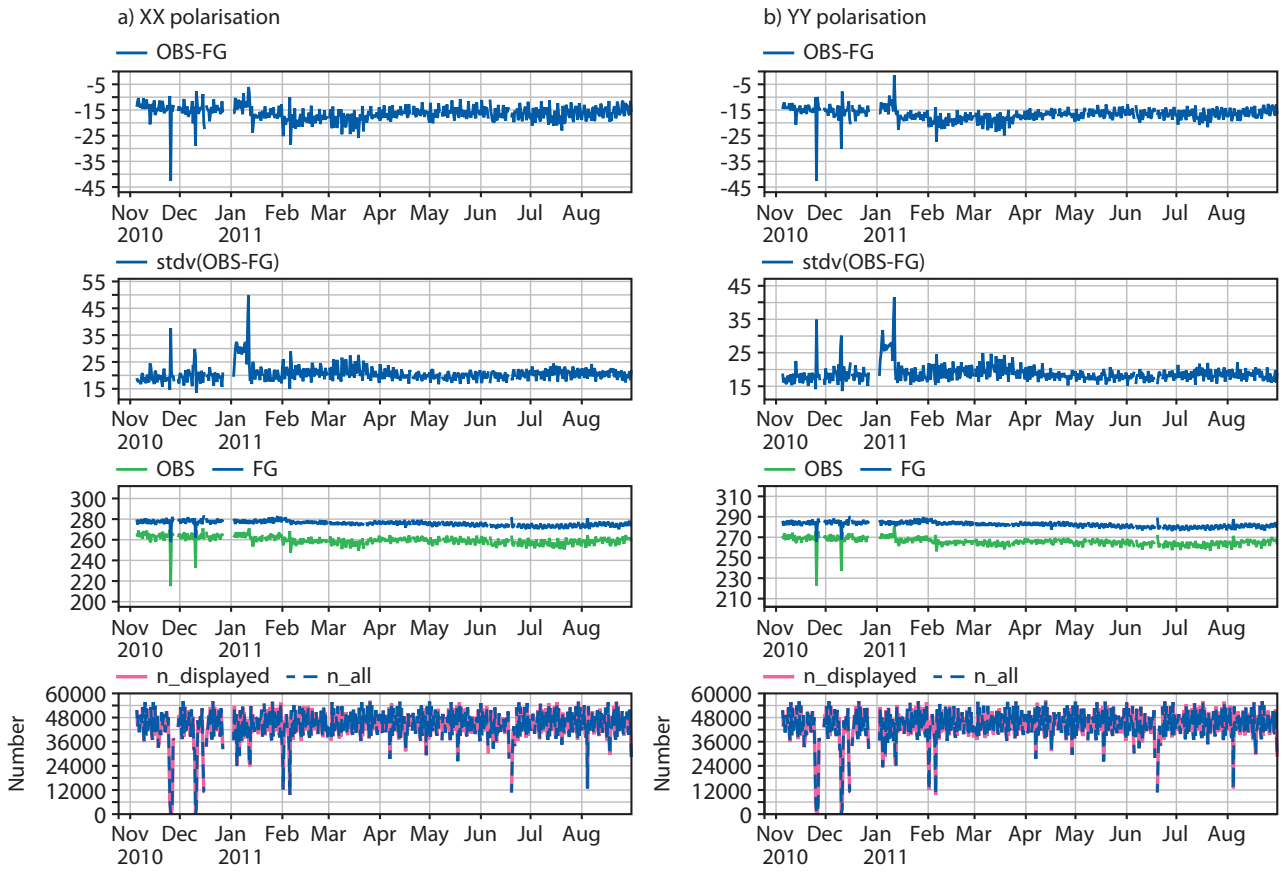

Figure 14: As in Fig. 8 but for South America.

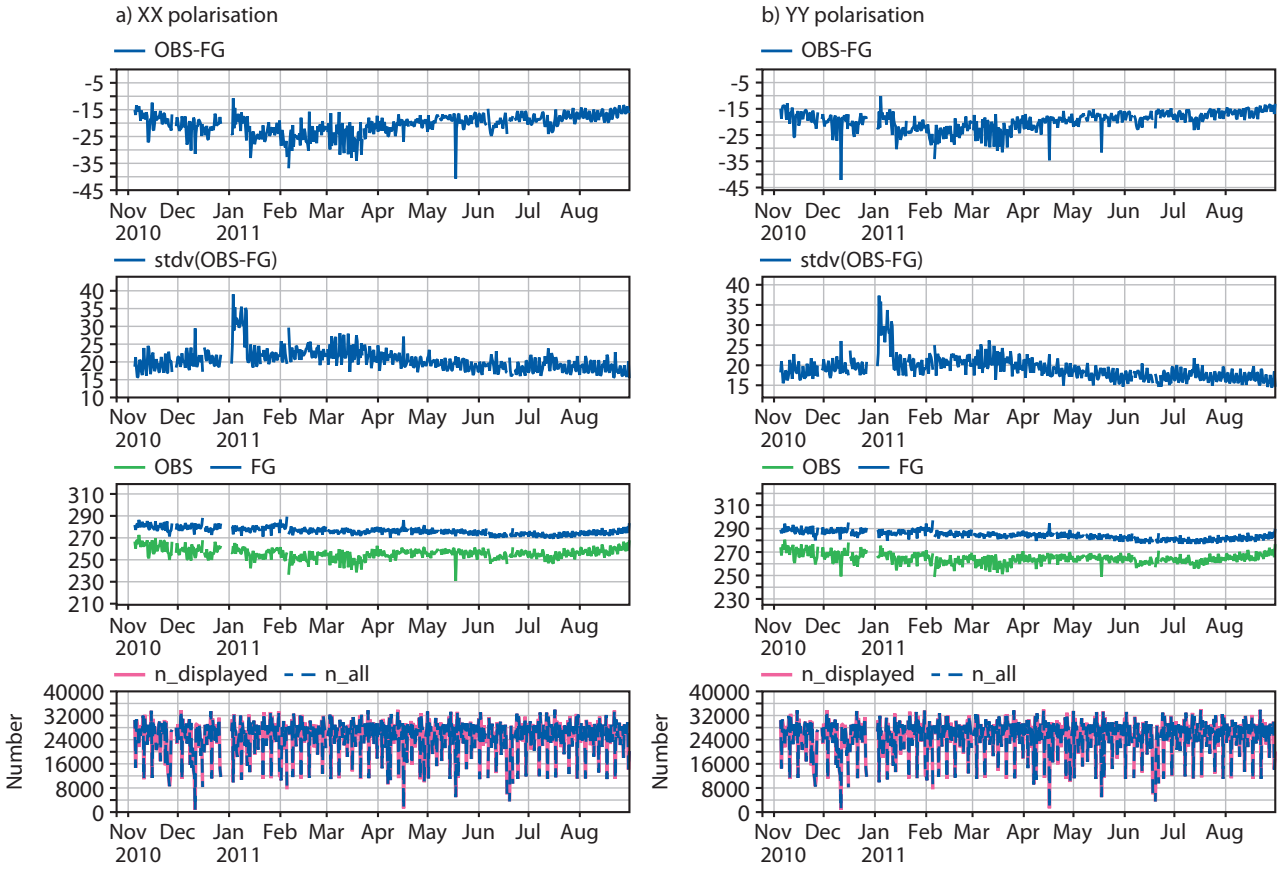

Figure 15: As in Fig. 8 but for Australia.

3.4 Angular distribution of bias

In section 3.3 an analysis of the bias was given at 40 degrees incidence angle. However the results presented can considerably change depending on the viewing angle. The most recent product incorporated in the ECMWF monitoring suite was the angular distribution of bias (named as 'scatter plots' in the website). In the case of SMOS they are important, as they provide a good insight into the bias as a function of the incidence angle. This section summarizes the averaged results obtained for 3 months of data, from August 2011 to the end of October 2011.

Fig. 16 presents the time and spatial averaged bias as a function of the incidence angle, at global scale for the Northern and Southern Hemispheres, and for XX and YY polarisations. Fig. 17 presents the angular distribution of bias for some regions: Europe, North America and Australia. The coloured scale bar refers to the number of observations within each level of bias. It is easily noticeable that the number of observations in Fig. 16 is much larger than in Fig. 17, especially near the zero bias, because the areas over which statistics are computed are much larger. At global scale the number of observations accounted for in these plots is greater than 254 millions, 146 millions for the Northern Hemisphere and 107 millions for the Southern Hemisphere, respectively. This gives an idea on the large number of observations obtained with SMOS, this despite that only observations whose incidence angles are multiples of 10 are included in these plots.

It is shown that, independently of the area shown, for YY polarisation the mean bias keeps the same trend as a function of the incidence angle. In this case they are maximum at 30 degrees (around -20 K) and minimum at 60 degrees (close to zero). For XX polarisation it is more dependent on the geographical area. The reason is likely the contamination by RFI sources. For example, in Fig. 16 it is observed that the relation between mean bias and incidence angle is very different for the Northern and Southern Hemispheres at the XX polarisation. However, the trend is increasing bias (in absolute value) with increasing incidence angle, being in most of the cases maximum at 60 degrees. In the case of Australia the bias are especially significant at 60 degrees for XX polarisation. In this case it is observed that very few departures are found greater than 20 K, whereas they can be as negative as -90 K. A good fraction of Australia is covered by deserts and many other pixels have a significant fraction of bare soil. The influence of the soil roughness on the simulated brightness temperatures is especially important here, and the CMEM current parameterisation of the roughness model will be revised accordingly.

From these figures it is observed that for both polarisations there are also a significant number of observations with large first-guess departures. These are mainly due to RFI sources, but they are not the only reason as explained in (Sabater et al. 2011b).

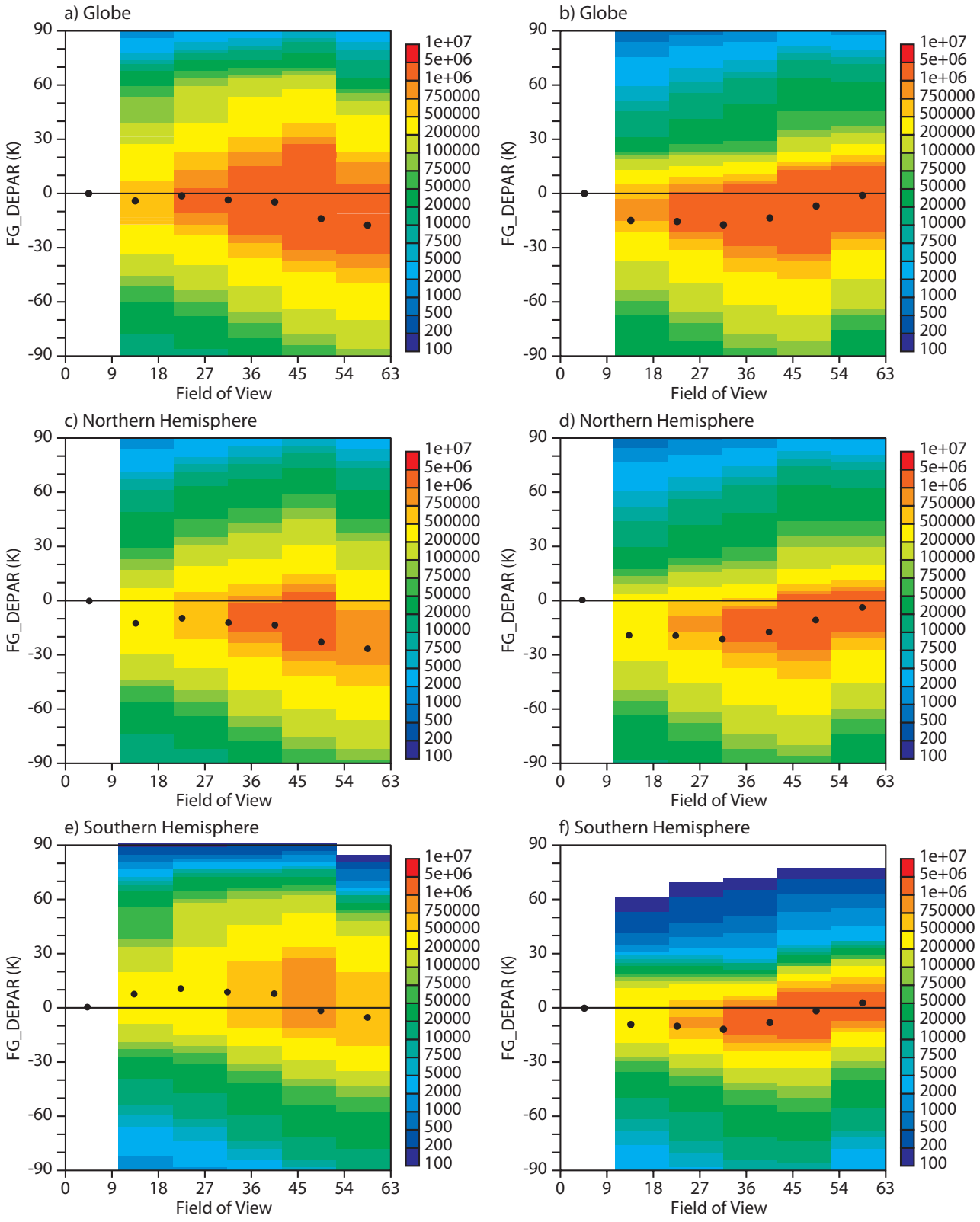

Figure 16: Mean bias as a function of the incidence angle for XX polarisation (left column) and YY polarisation (right column). The period considered spans from 6 August to 3 November 2011. Only continental surfaces are considered in these figures.

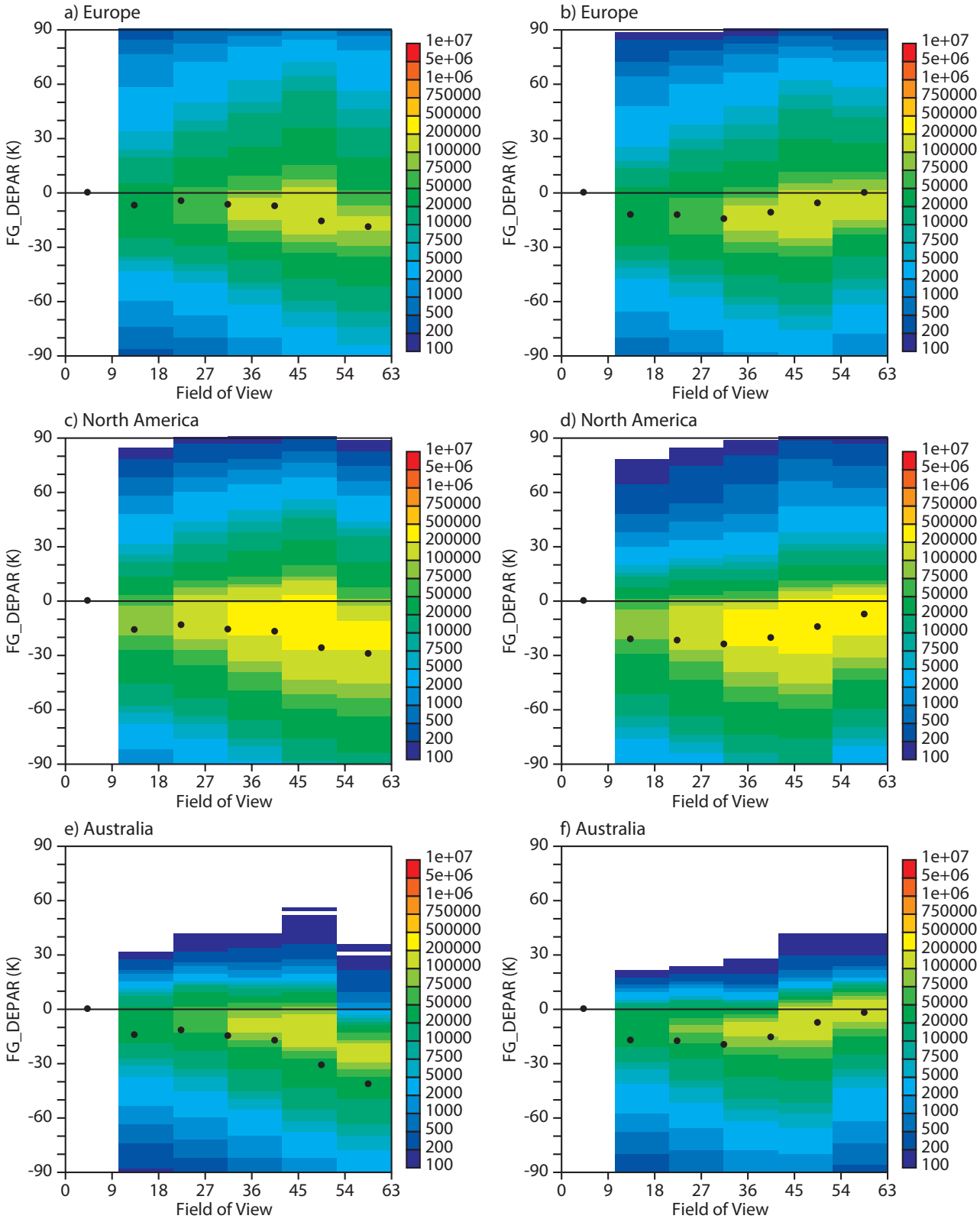

Figure 17: As Fig 16 but for Europe, North America and Australia.

3.5 Hovmöller plots

Hovmöller plots produce one mean value averaged per predefined band of latitudes as a function of time. So they provide a latitudinal-temporal perspective of several statistical variables and thus, they make it possible to analyse the seasonal evolution of averaged values per latitude band. Punctual problems in the data that could be unnoticed in time-averaged geographical plots can be easy identified in these plots.

In Fig. 18 the evolution of the averaged brightness temperatures per band of 2.5 degrees of latitude are shown for one year (November 2010 - November 2011). The seasonal evolution of brightness temperatures per band of latitude is clearly shown for both polarisations, increasing towards the Northern Hemisphere from May until August and increasing in the Southern Hemisphere the rest of the year. Maximum values are always obtained in the tropics. A strong difference is observed in the mean brightness temperatures between 20 and 60 degrees incidence angles, with a mean difference for both polarisations of about 20 K.

First-guess departures are presented in Fig. 19. The area covered by snow is clearly seen in the XX polarisation, as the emission over snow is currently strongly underestimated, so large departures are obtained in this zone. It is observed that the maximum of snow cover is obtained between mid January and mid February, with snow down to 30 degrees North. At 60 degrees incidence angle, the model clearly overestimates the observations for XX polarisation, except the areas around the Equator where the model is much closer to the observations. This is likely due to a current accurate representation of dense vegetated canopies. The white line around 60 degrees South is due to the absence of land points. The emission over the poles is also underestimated for both polarisations and all incidence angles.

The contamination produced by intermittent sources of RFI are clearly seen in Fig. 20. This figure shows the standard deviation of the first-guess departures. A red, non-uniform strip, corresponding to large variability of the first-guess departures is observed between 20 and 40 degrees North. They are mainly caused by RFI. However, they are not the only reason causing these large departures, also the presence of snow and ice contributes. In the time series plots (section 3.3) a larger variability of the observed brightness temperatures over snow and ice covered areas was observed, which increases the variability of the bias. For example, in the XX polarisation it is clearly seen that the first-guess departures standard deviation is lower between 20 and 40 degrees North during the Boreal summer months. Likewise, at 60 degrees incidence angle for XX polarisation, larger departures between 45 and 55 degrees South are observed, very likely due to the presence of the Patagonian ice sheet.

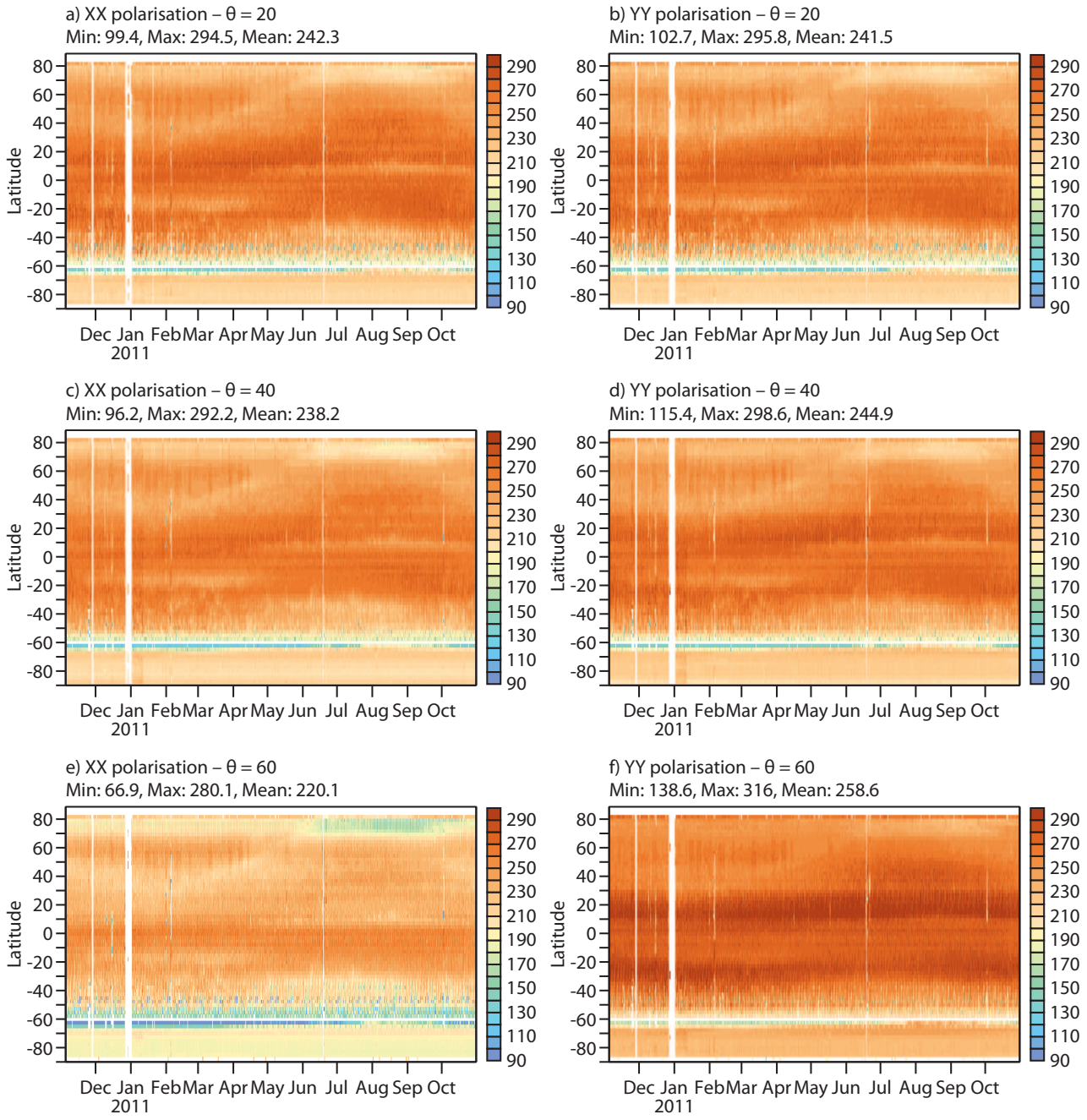

Figure 18: Mean SMOS observed brightness temperatures per bands of 2.5 degrees of latitude as a function of time. Left panel if for XX polarisation and right panel for YY polarisation. Figures are shown for 20, 40 and 60 degrees incidence angle.

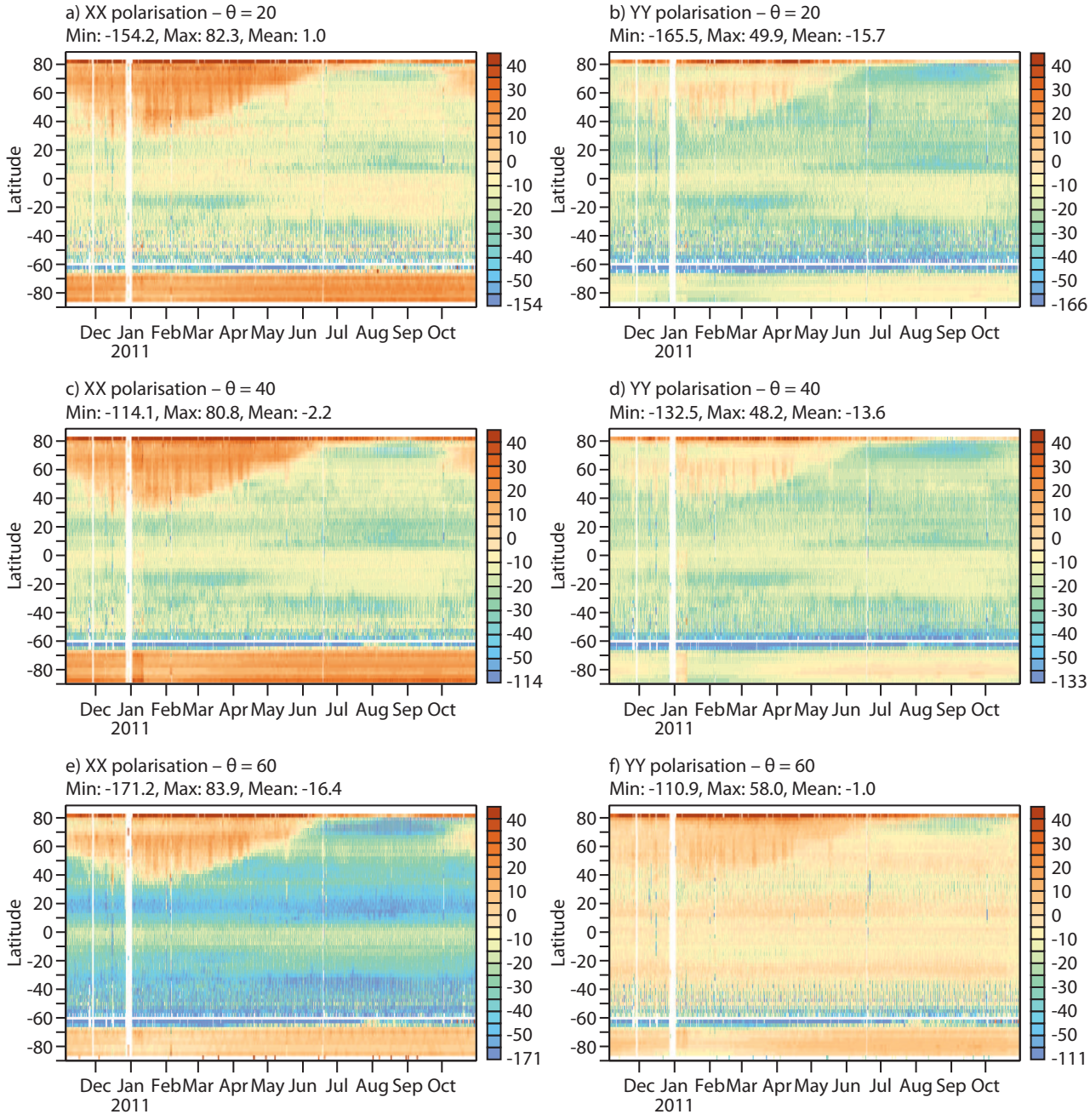

Figure 19: As in Fig. 18, but the variable shown is the first-guess departures.

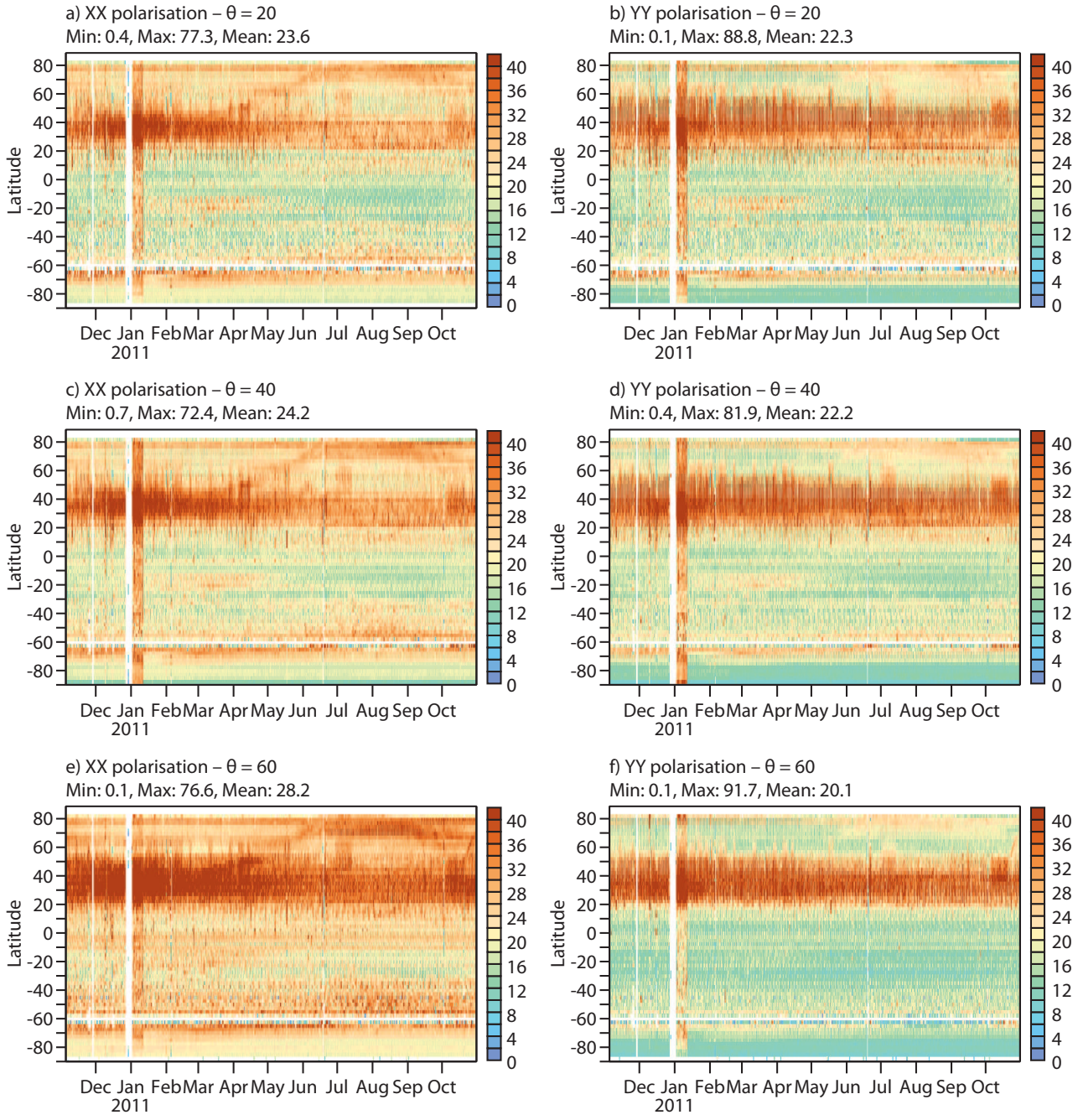

Figure 20: As in Fig. 18, but the variable shown is the first-guess departures standard deviation.

4 Monitoring over ocean

In this section some of the more relevant results obtained with the monitoring suite [see a description in part III of (Sabater et al. 2010) and (Sabater et al. 2011b)] over oceans are presented.

4.1 Simulations of brightness temperatures

The SMOS monitoring suite developed at ECMWF (Sabater et al. 2010) produces daily statistics not only for continental surfaces, but also for oceans. The CMEM forward operator introduced in section 3.1 is also used to simulate brightness temperatures over oceans surfaces. The emissivity over oceans in the L-band is currently modelled in CMEM in a very simple way. It considers the ocean as a smooth surface, the influence of the wind and the galactic noise are not accounted for. For the dielectric constant computation, a difference is done between liquid water or pure ice. As effective temperature, the sea surface temperature is used.
Thus, the results presented from figures 21 to 35 should be considered as preliminary. A future implementation of the roughness and galactic noise contributions to the total brightness temperatures at the top of the atmosphere will make it possible to get more robust conclusions over oceans.

4.2 Time-averaged geographical mean fields.

Fig. 21 and Fig. 22 show the averaged brightness temperatures over ocean surfaces as a function of incidence angle for August 2011 and for XX polarisation (Fig. 21) and YY polarisation (Fig. 22). Each value represents a mean value in boxes of 0.25 degrees. As it occurs over continental surfaces, brightness temperatures increase with the incidence angle for YY polarisation and decrease for XX polarisation, with values notably lower than over land, on average 120 K lower for August 2011. The YY polarisation has a larger angular dynamical range, of about 30 K larger in average than the XX polarisation between 20 and 60 degrees. August is a winter month at the Southern Hemisphere and around the Antarctica the ocean is frozen. This is clearly seen in these figures as the emissivity is much larger, and therefore the observed brightness temperatures. Also for the North Pole brightness temperatures are significantly larger. Given that oceans are much more homogeneous than continental surfaces, the map of brightness temperatures over oceans are relatively homogeneous in comparison to land surfaces. Large inland water bodies (mainly lakes) are also clearly visible. For August 2011 the CMEM model largely overestimates the brightness temperatures over lakes.

The evolution of the SMOS observed brightness temperatures standard deviation, from November 2010 to August 2011 (one averaged value per month), is shown in Fig. 23. It is shown only at 40 degrees incidence angle and for XX polarisation. Fig. 24 is the equivalent figure for YY polarisation. The spatial sampling is 0.25 degrees. The spatial monthly average of brightness temperatures standard deviation is more than 14 K for XX polarisation and slightly lower for YY polarisation. Anomalous large values are observed for January 2011 which, as mentioned earlier in this report, are due to the degradation of the science data during the period following the thermal stability test of the instrument at the end of 2010. These figures show clearly the contamination of RFI land sources into the oceans. Near China, Middle East and Eastern European coastlines the standard deviation of brightness temperatures is very large, which is due to RFI. But RFI also affects areas much further from the coasts, although in a lesser extent. Especially interesting is the case of Europe. In both polarisations it can be observed that the progress made at shutting down illegal RFI sources in Europe has had a direct influence over oceans near the coasts. In the figure for August 2011 the Western European coastline appears very clean in contrast to previous months where the RFI situation was still quite bad.
The other interesting feature observed in these figures is the transition zone between frozen and liquid water over Antarctica. Frozen and liquid water have very different dielectric properties, and therefore they present very different emissivities. As this is a very sensitive and dynamical zone, the variability of brightness temperatures is very large. During the summer months at the Southern Hemisphere this transition zone can barely be observed, or at least is very close to the Antarctica continent, whereas it moves far from the coastline during the winter months.

Figs. 25 and 26 show the evolution of the first-guess departures (observed brightness temperatures minus the CMEM model equivalents) over oceans, at the antenna reference frame from November 2010 to August 2011 (one averaged value per month), at 40 degrees incidence angle, and for XX and YY polarisation, respectively. For the bulk of the oceans the first-guess departures look very systematic and they have a narrow dynamical range variability, lower than 10 K. They are quite constant for all months which is also partly a consequence of the current limitations of the emission model over oceans. Simulated brightness temperatures are underestimated for XX polarisation, slowly increasing in the North Hemisphere towards the summer months. The situation is just the opposite for YY polarisation, as the model systematically overestimates the observations and the best spatial agreement is found in July 2011. Near the poles, with frozen water and snow, the first-guess departures also have a very different behaviour.

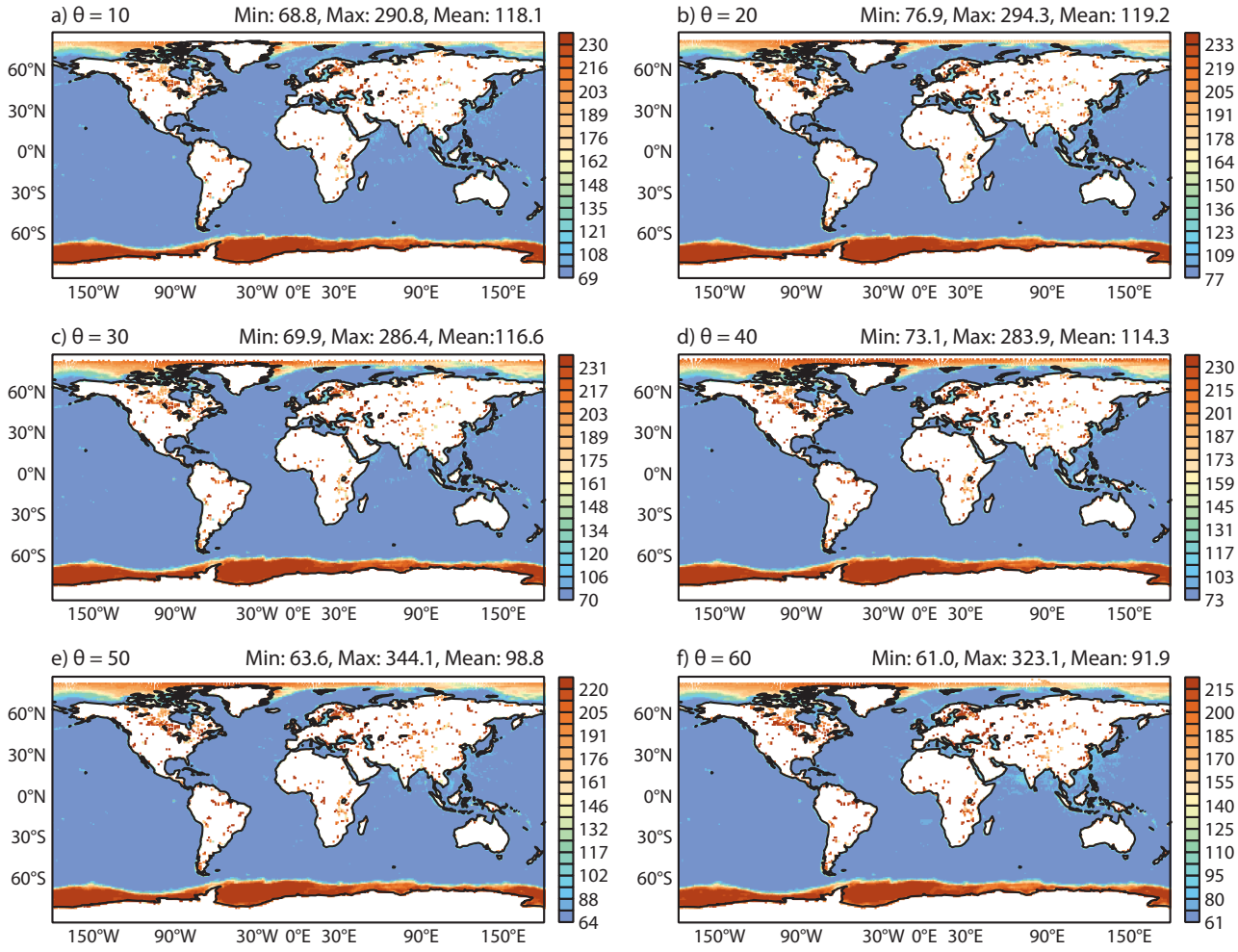

Figure 21: August 2011, angular global mean of the SMOS observed brightness temperatures for ocean surfaces and for XX polarisation. Each value represents a mean value of all the data inside a box of 0.25 degrees.

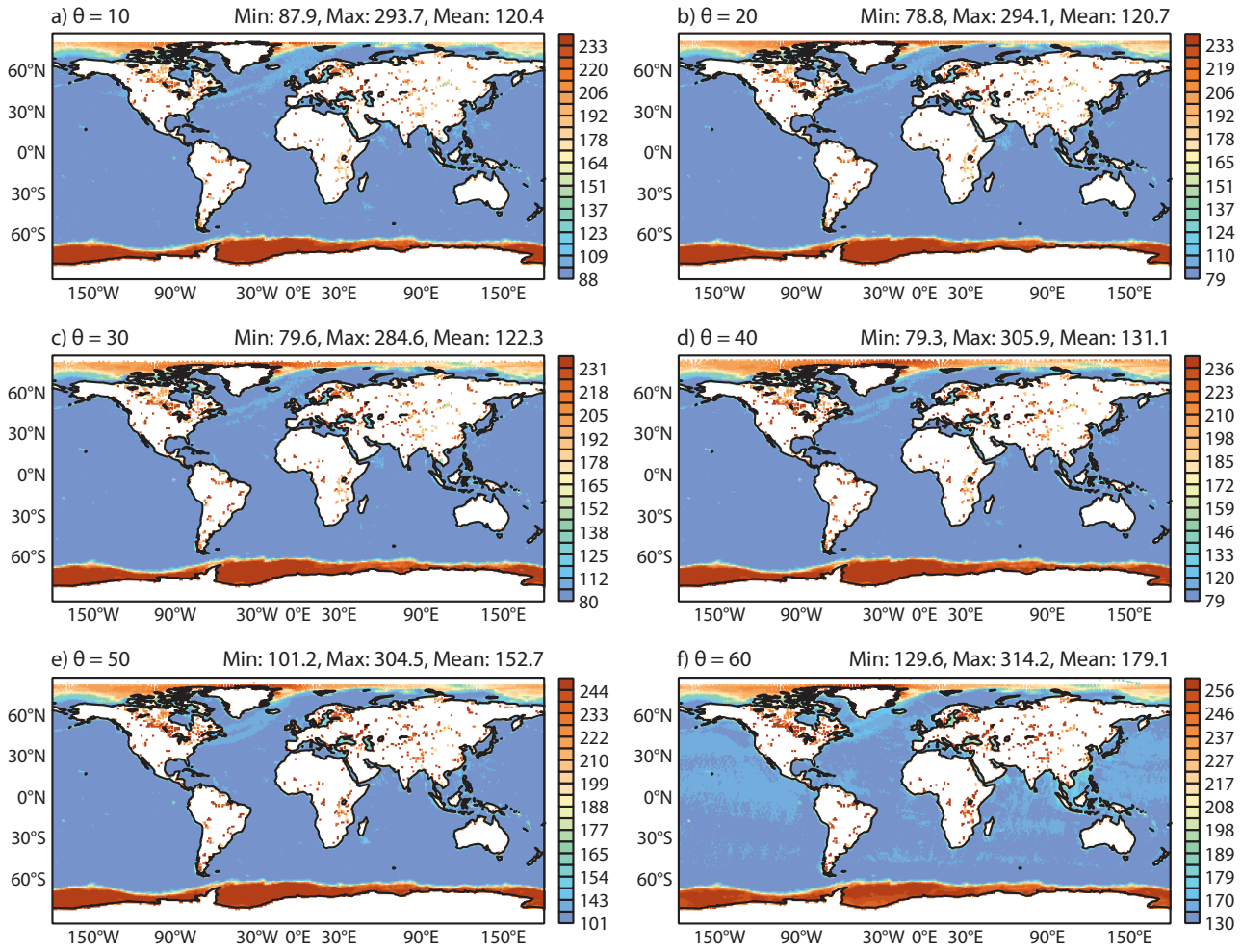

Figure 22: As in Fig. 21 but for YY polarisation.

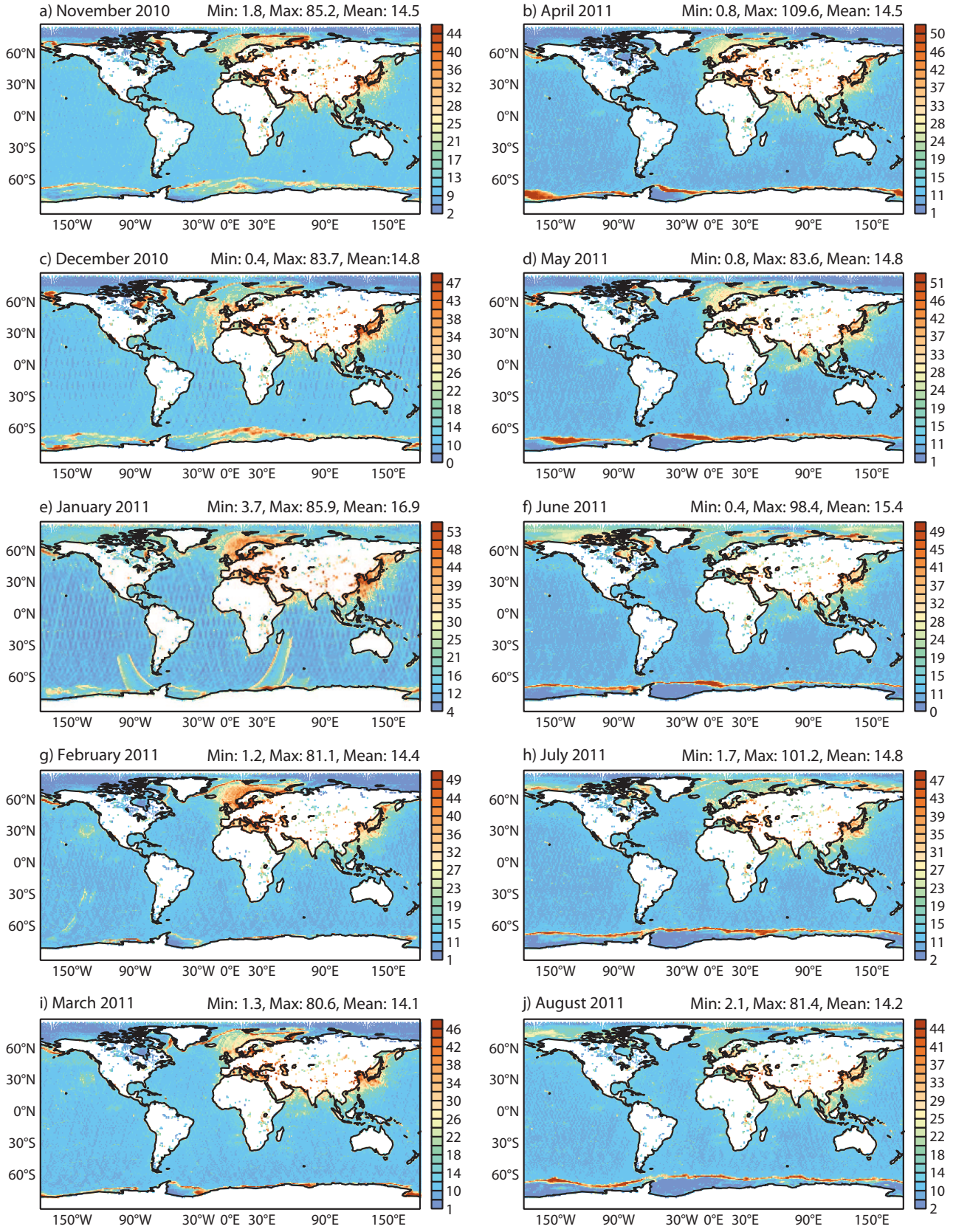

Figure 23: Monthly mean of the SMOS observed brightness temperatures standard deviation, for XX polarisation and for ocean surfaces only. Each value represents a mean value of all the data inside a box of 0.25 degrees. The incidence angle is 40 degrees.

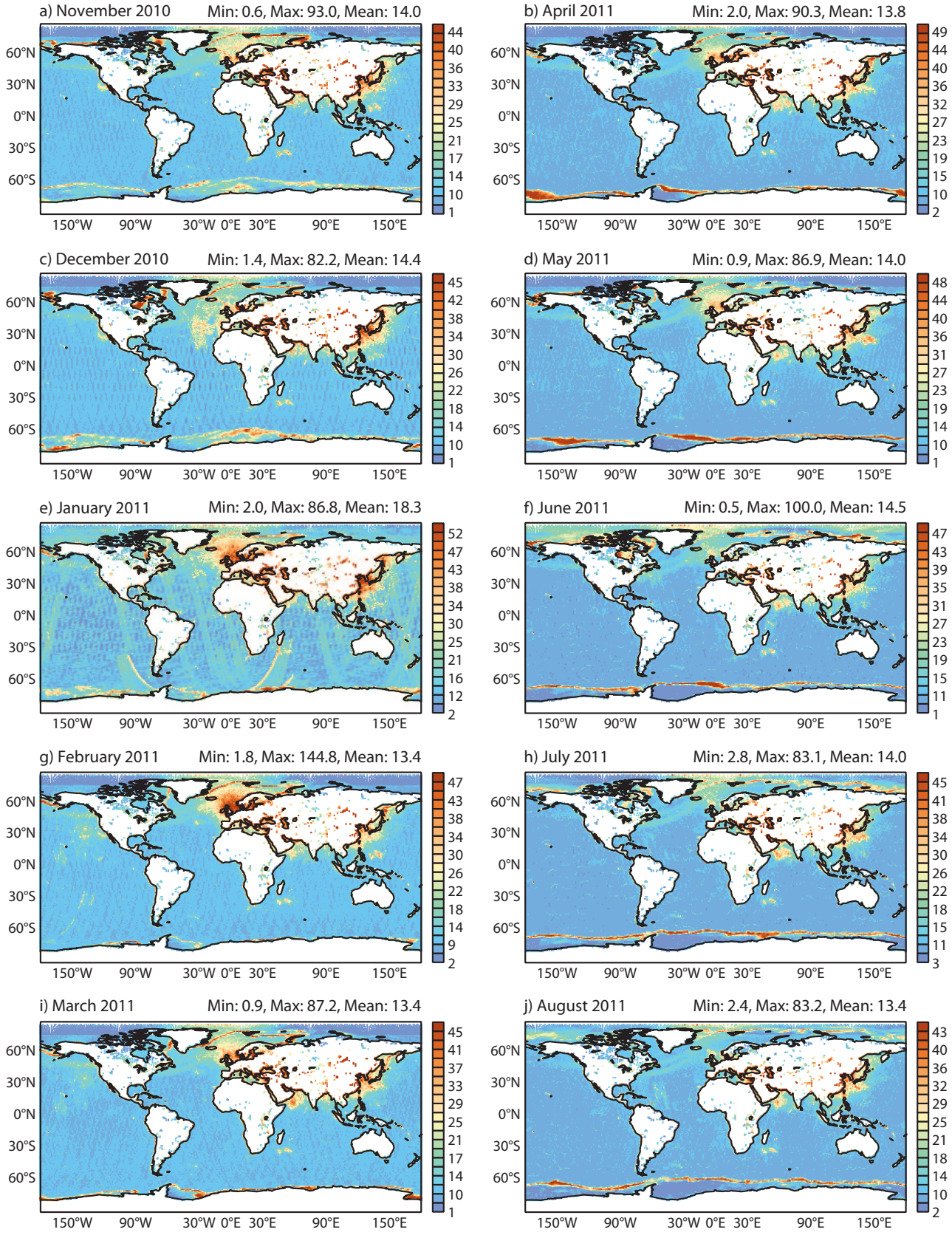

Figure 24: As Fig. 23 but for YY polarisation.

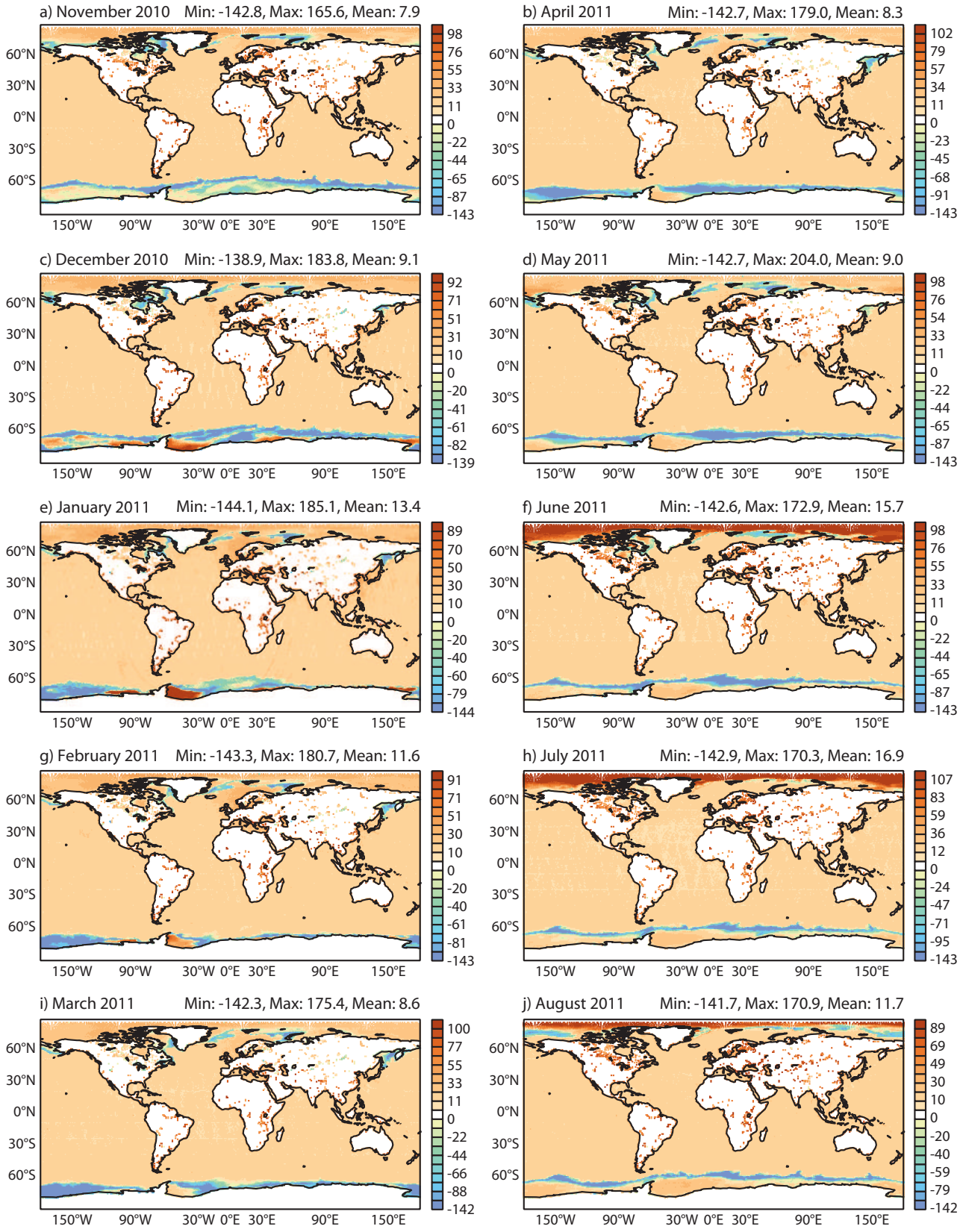

Figure 25: Monthly mean of the first-guess departures between SMOS observed brightness temperatures and the CMEM modeled equivalents, for XX polarisation and 40 degrees incidence angle.

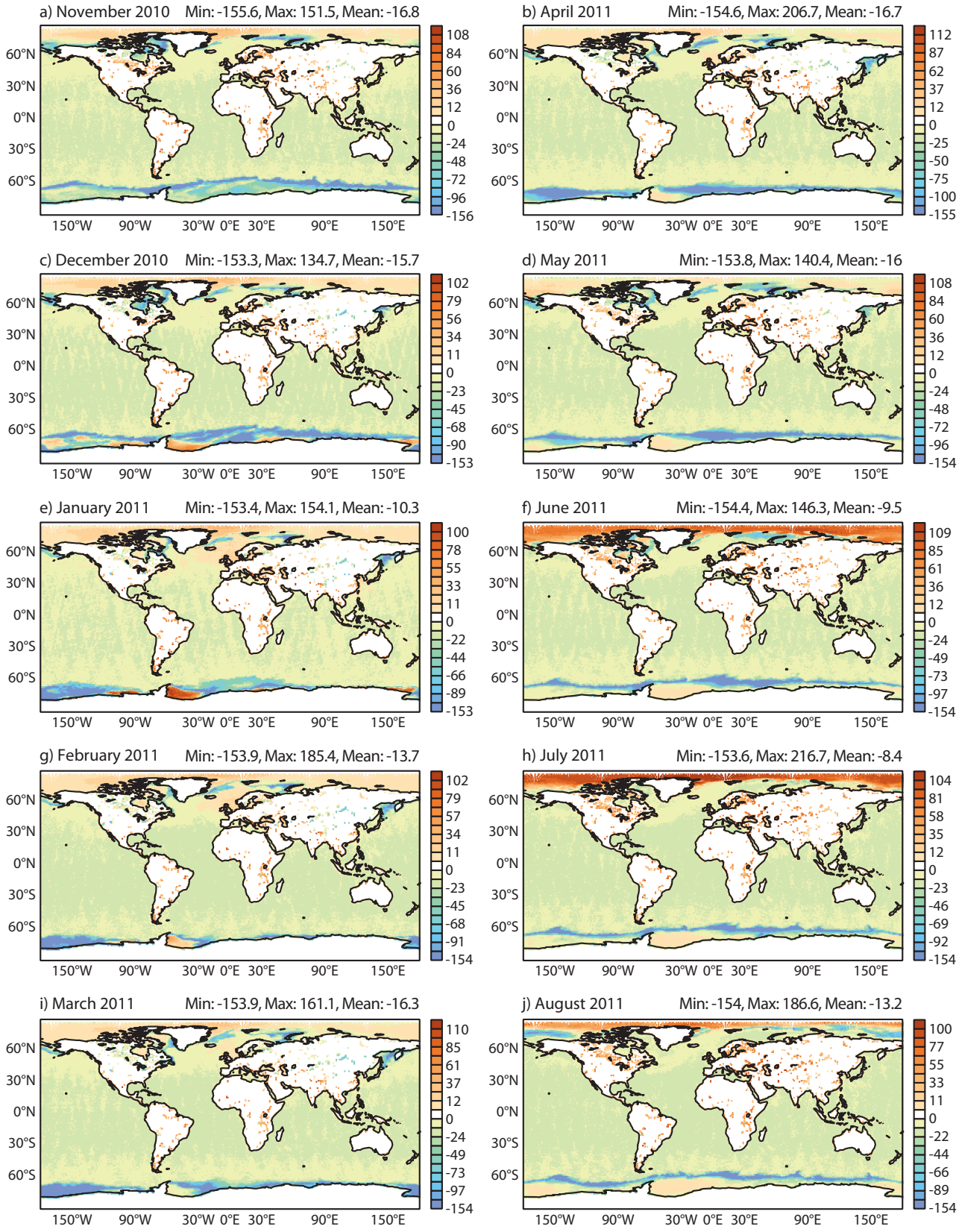

Figure 26: As in Fig. 25 but for YY polarisation.

4.3 Time series

Figs. 27 to 29 present the time series of the observed brightness temperatures, CMEM modeled equivalents, first-guess departures and number of observations, from November 2010 to August 2011. This is presented only over ocean surfaces, at global scale, for the North Hemisphere and the South Hemisphere, respectively. They are produced at 20 degrees incidence angle. Figs. 30 to 32 show the equivalents results for 50 degrees incidence angle. Each value represents one mean value per ECMWF 4DVAR 12 hours assimilation cycle. These are only preliminary results and the influence of the wind and the galactic noise are not included in these time series.

With the current simulation of emissivities over oceans, either for XX or YY polarisation, there is a quite similar seasonal cycle of bias at global scale, with a peak between June and July and a minimum between October and November. However, as the bias are constantly negative for YY polarisation, the peak in June-July means that in absolute value bias are lower. First-guess departures standard deviations are very large, around 35 K for both polarisations and increasing rapidly from mid-May until end of June. Both, bias and observations standard deviations present the same seasonal cycle. By looking at Fig. 28 (Northern Hemisphere) and 29 (Southern Hemisphere) it can be observed that the peak of bias between June and July clearly comes from the North Hemisphere and the peak at the end/beginning of the year comes from the Southern Hemisphere behaviour. The previous results are for 20 degrees incidence angle, but bias are however very dependent on the incidence angle. Figs. 30 to 32 show the previous time series, but for 50 degrees incidence angle. At global scale the bias distribution is almost the opposite of the 20 degrees incidence angle results, i.e., now the model mostly overestimates the observations at the XX polarisation and underestimates them at the YY polarisation. However, the shape and the peaks are equally found at the same time of the year. As it happened for land pixels, the thermal stability test of the SMOS platform that took place at the end of December 2010 yield anomalous results at the beginning of January 2011.

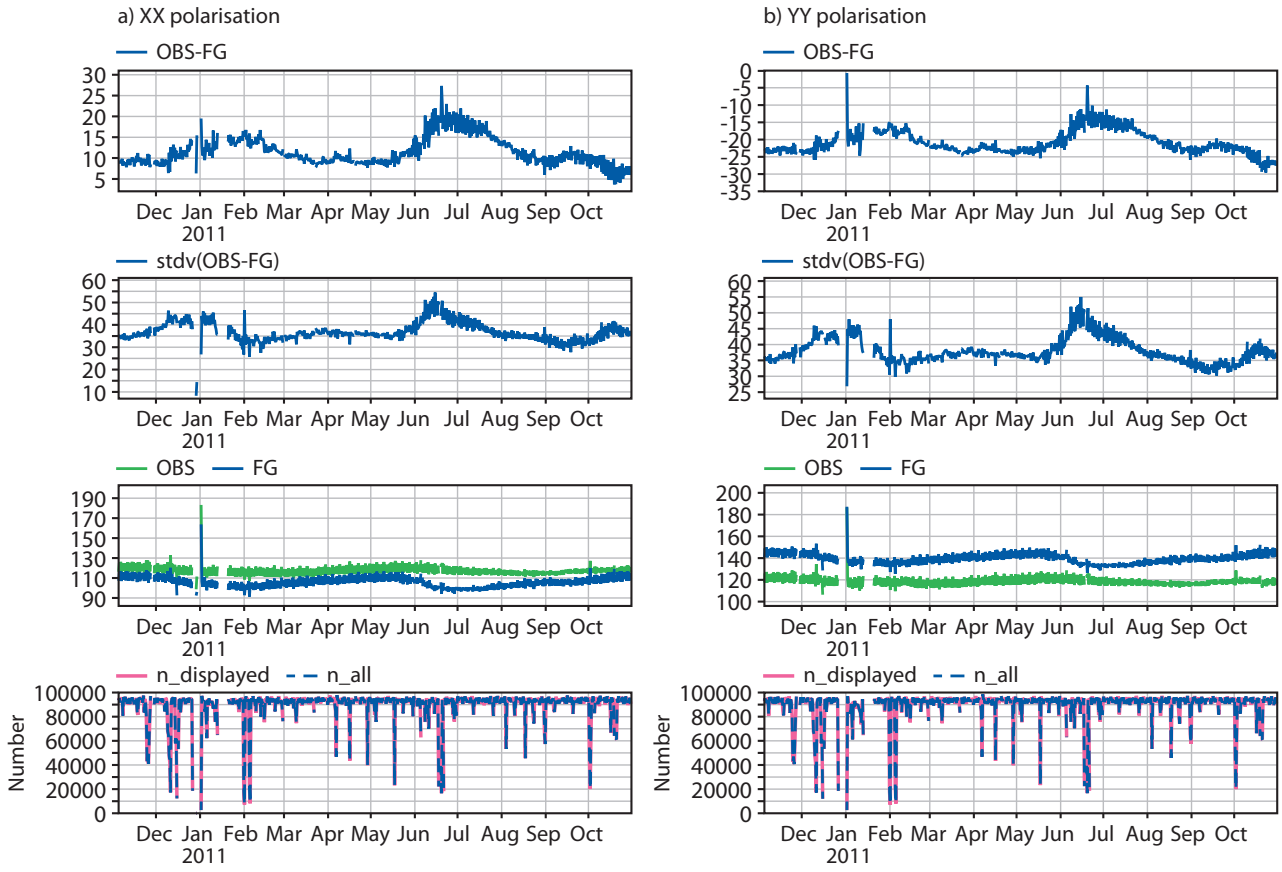

Figure 27: Global scale, time series from November 2010 to August 2011 over oceans, at 20 degrees incidence angle, of mean bias (top figures), mean standard deviation of bias (second top row), comparison between observed brightness temperatures and the CMEM model equivalents (third row), and number of observations (bottom figures). Each value is an averaged value per ECMWF 4DVAR 12h cycle. Left panel is for XX polarisation, right panel for YY polarisation.

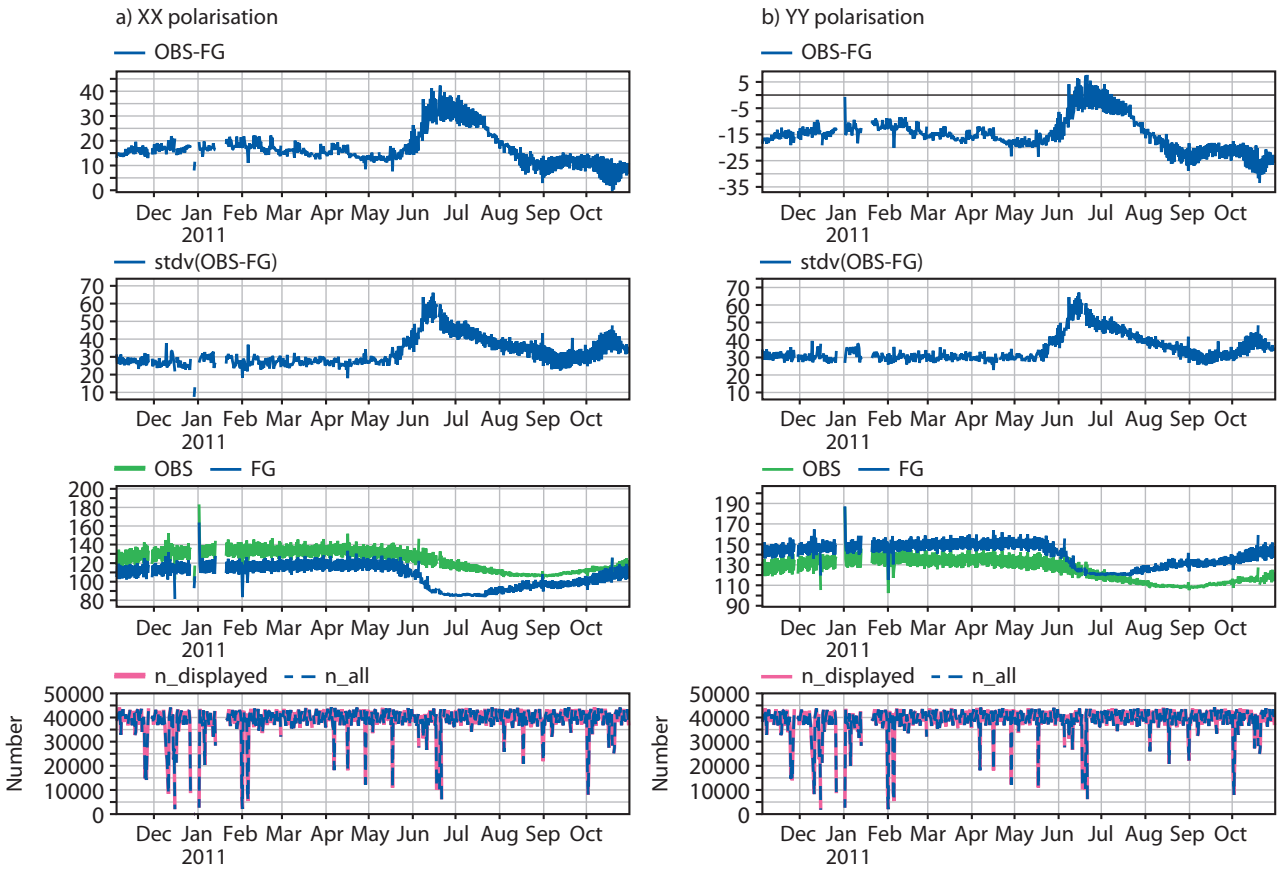

Figure 28: As in Fig. 27 but only for the oceans at the North Hemisphere.

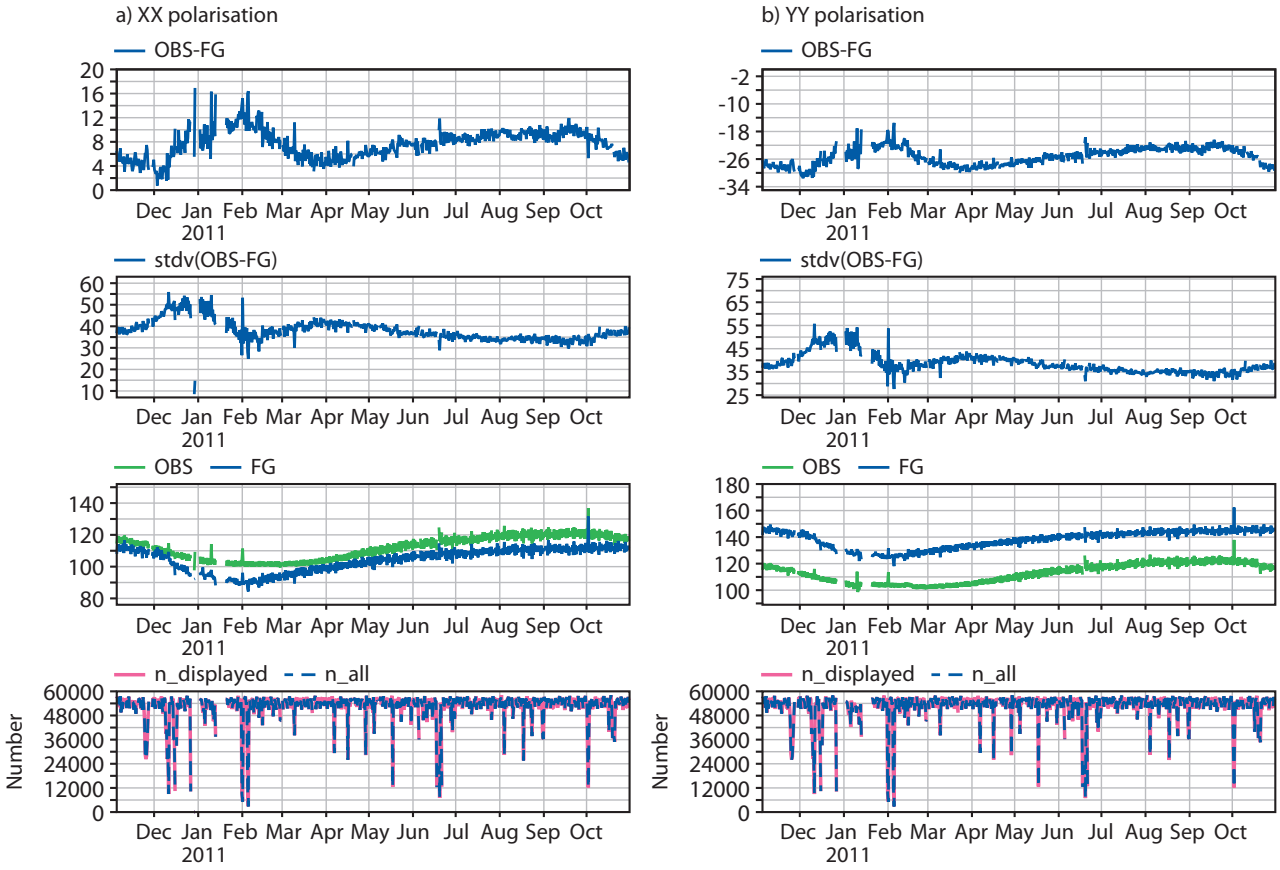

Figure 29: As in Fig. 27 but only for the oceans at the South Hemisphere.

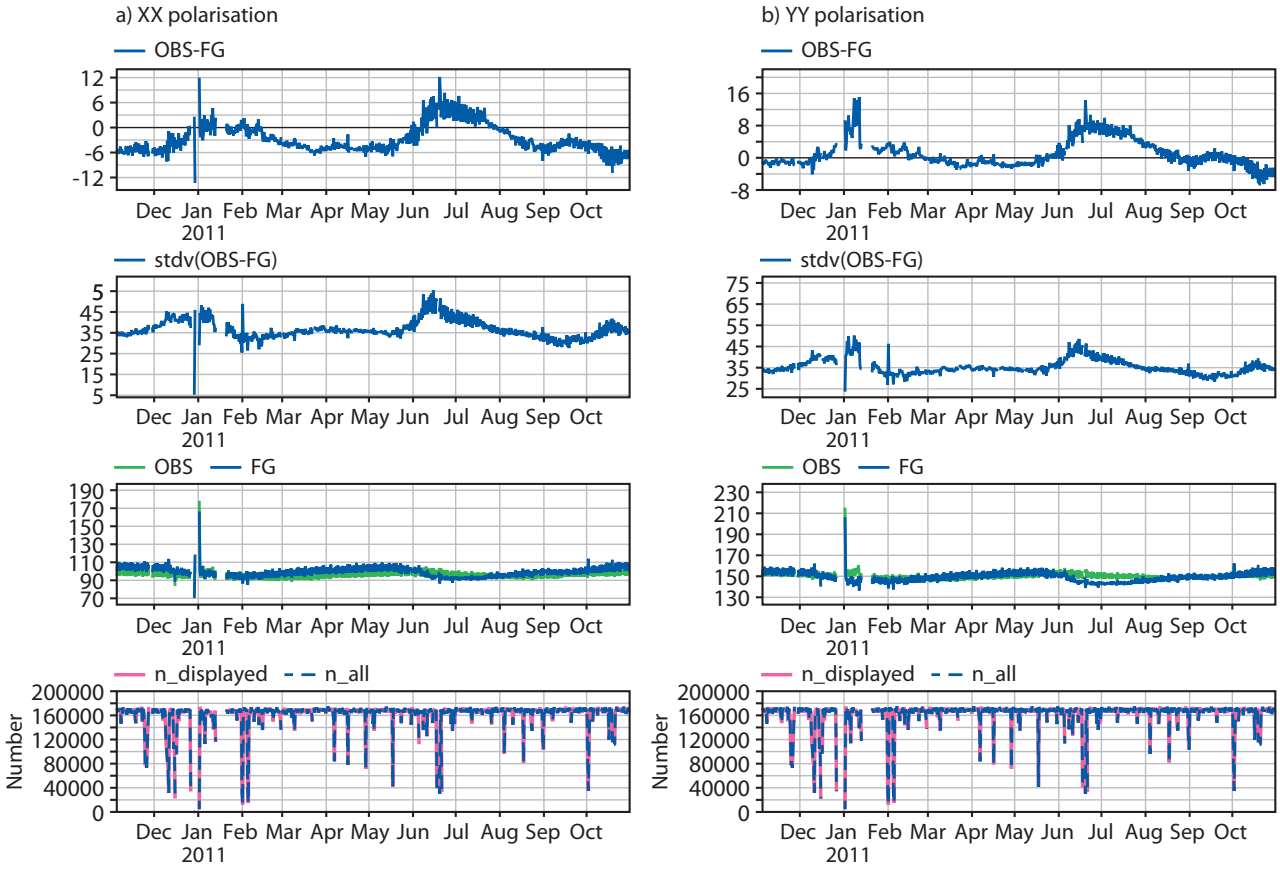

Figure 30: As in Fig. 27 but at 50 degrees incidence angle

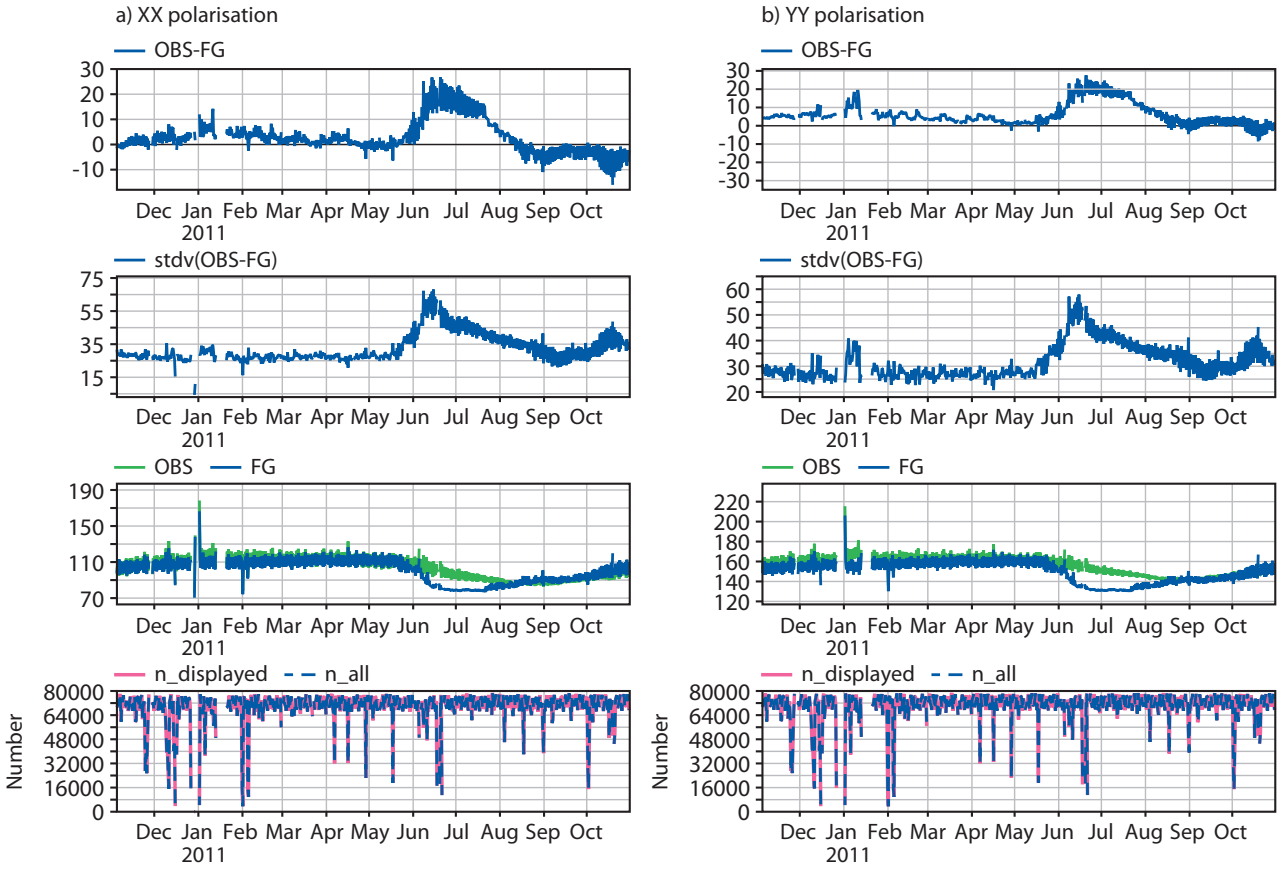

Figure 31: As in Fig. 27 but at 50 degrees incidence angle and only for oceans at the North Hemisphere.

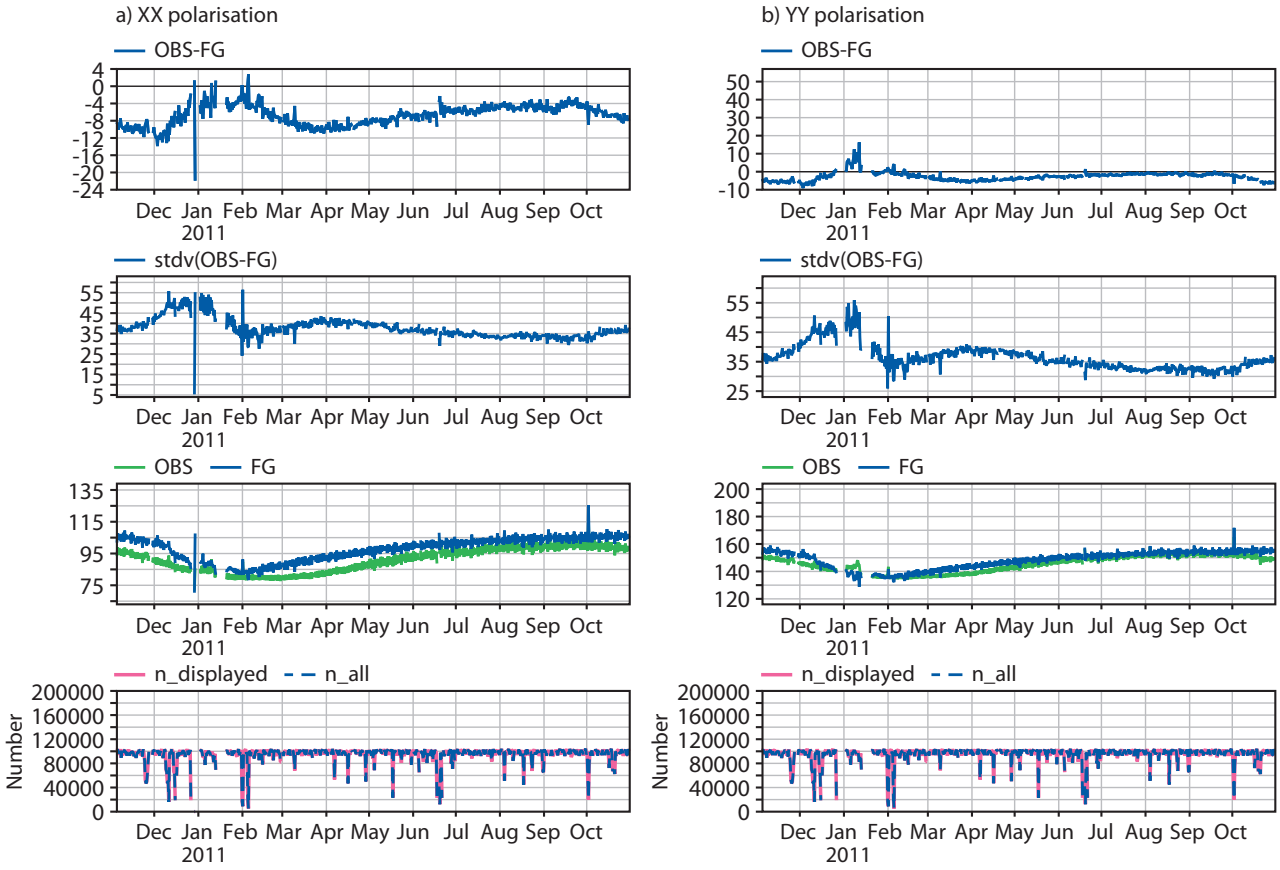

Figure 32: As in Fig. 27 but at 50 degrees incidence angle and only for oceans at the South Hemisphere.

4.4 Hovmöller plots

As it was done for the continental surfaces, Figs. 33 to 35 show the latitudinal-temporal evolution of the observed brightness temperatures, first-guess departures and standard deviation of first-guess departures, respectively, averaged per bands of 2.5 degrees of latitude from November 2010 to November 2011. They are produced at 20, 40 and 60 degrees incidence angle and for XX and YY polarisations.

In Fig. 33 the evolution of the fraction of frozen sea around the poles can be clearly followed as they present constrasting larger brightness temperatures than the rest of the seas. It was maximum in March 2011 at the North Hemisphere and in September 2011 at the South Hemisphere. Brightness temperatures clearly decrease with the incidence angle for XX polarisation while they increase for YY polarisation at a higher rate. With the current parameterisation of CMEM first guess departures are quite homogeneous over oceans (Fig. 34), with a variability lower than 2 K in general (Fig. 35). The polar areas have a contrasting different behaviour, with stronger departures and large standard deviations in the transition area frozen-liquid water.

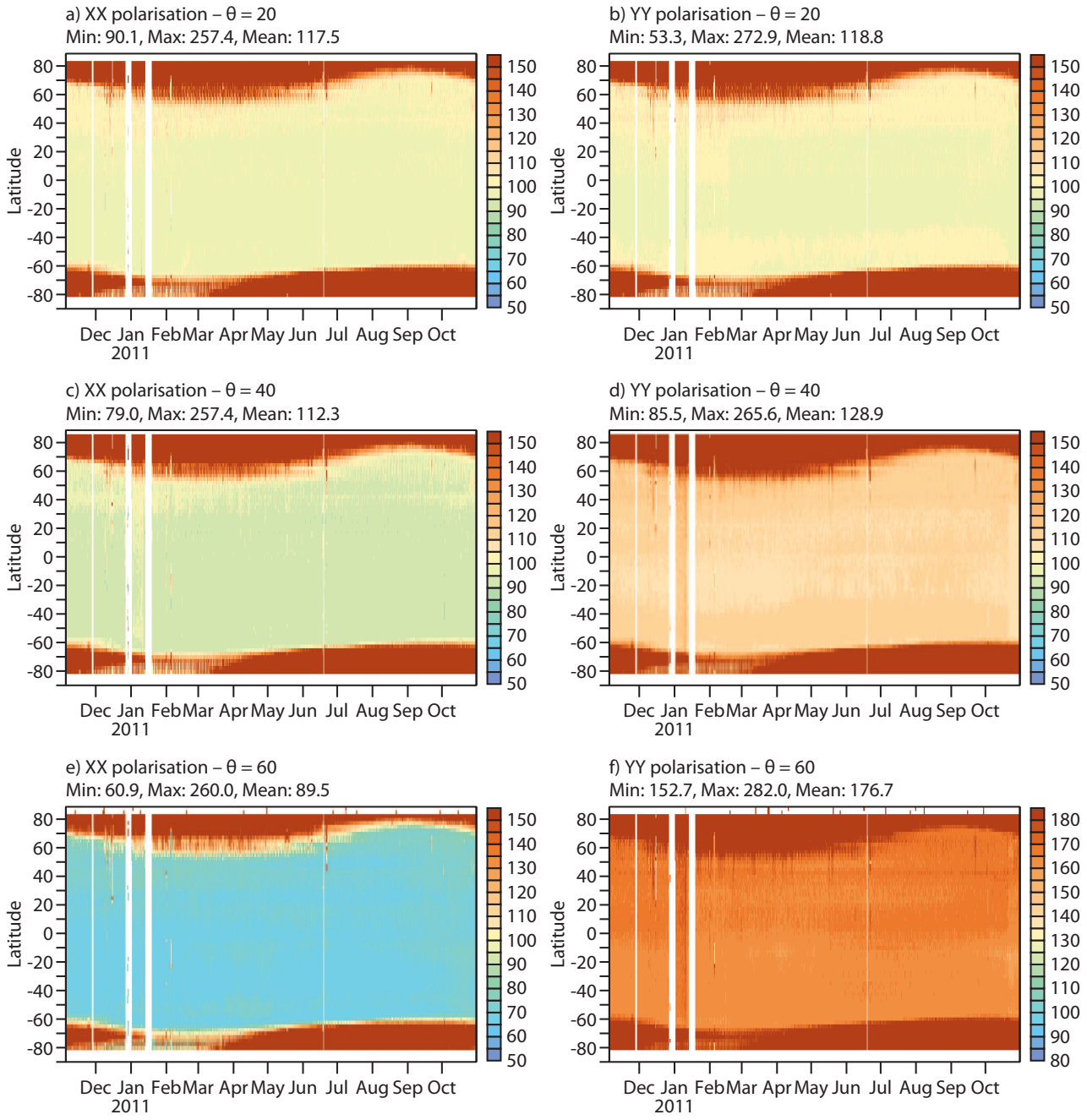

Figure 33: Mean SMOS observed brightness temperatures per bands of 2.5 degrees of latitude as a function of time, only over oceans. Left panel if for XX polarisation and right panel for YY polarisation. Figures are shown for 20, 40 and 60 degrees incidence angle.

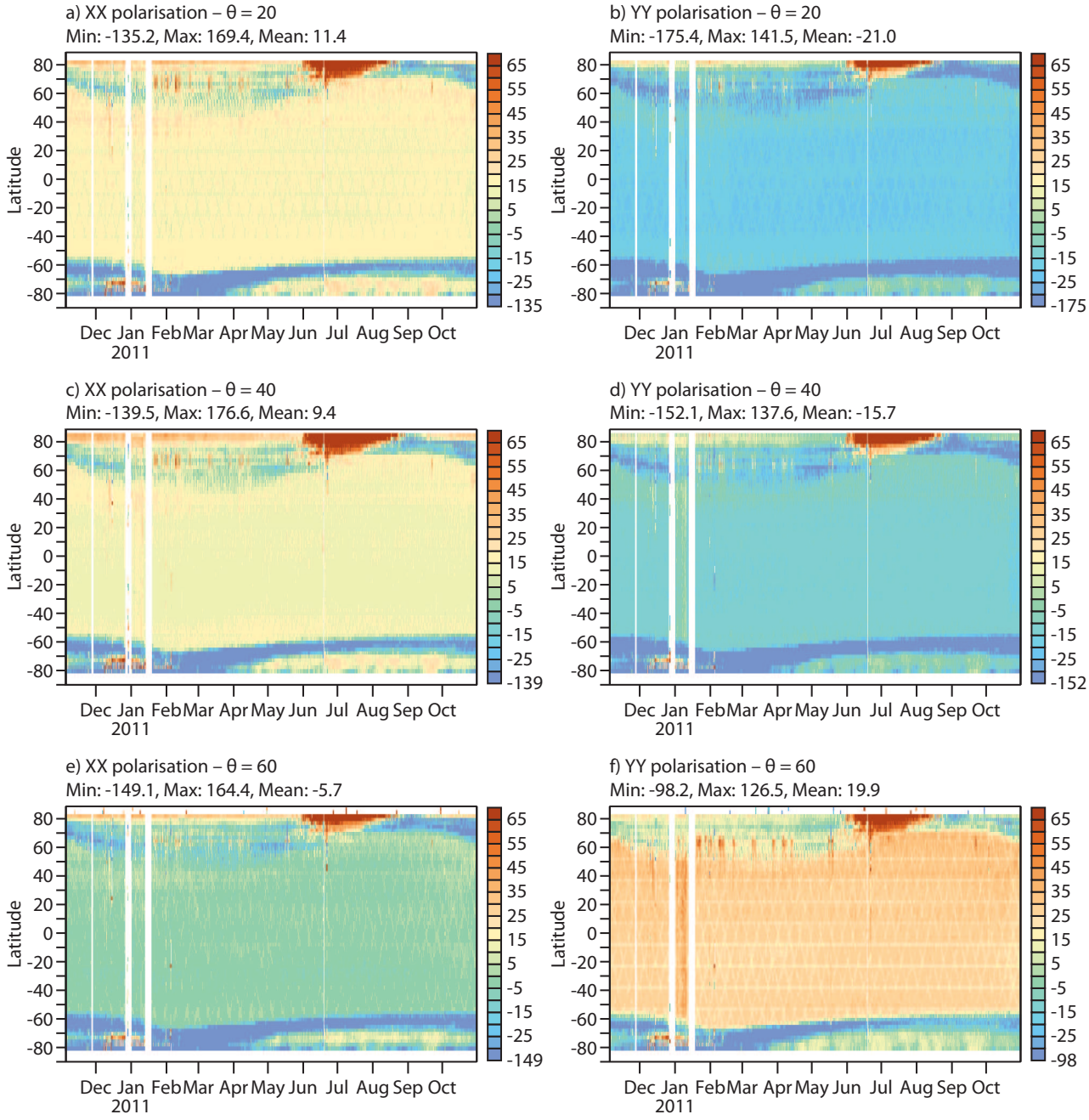

Figure 34: As in Fig. 33, but for the variable shown is the first-guess departures.

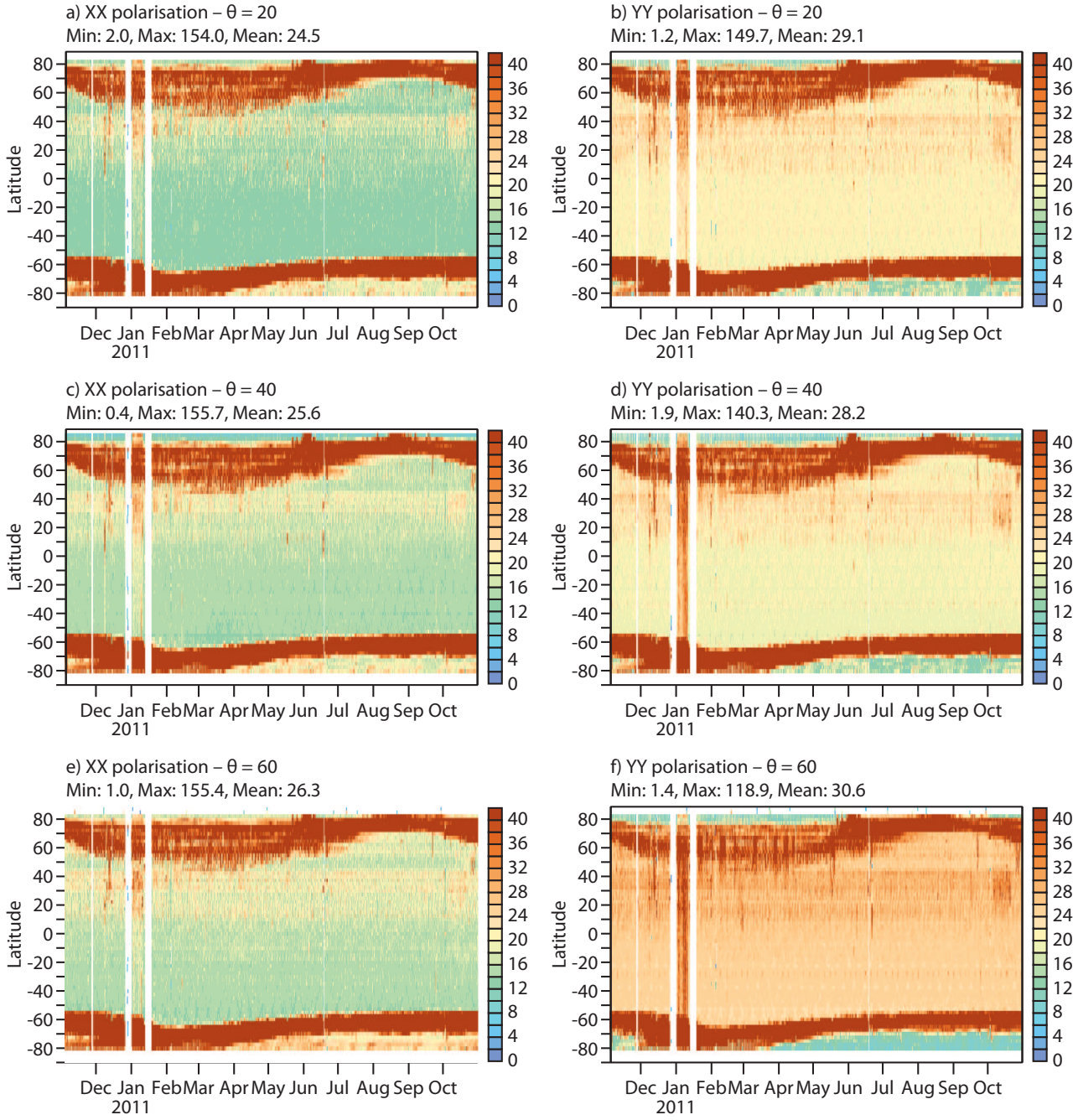

Figure 35: As in Fig. 33, but for the variable shown is the first-guess departures standard deviation.

5 Summary

This second SMOS monitoring report presents some of the Near Real Time SMOS monitoring results obtained for the period November 2010- November 2011. The ECMWF passive microwaves emission model CMEM is used to simulate brightness temperatures at the top of the atmosphere. Geolocated SMOS observed brightness temperatures are compared to CMEM values at the satellite antenna reference frame and in NRT. A whole annual cycle of statistical variables was computed and analysed.

Observed brightness temperatures behave as expected. Over continental surfaces RFI contamination is clearly seen in most of the figures. The brightness temperatures standard deviation present large anomalous values mainly over China, Middle East and Eastern Europe, with the YY polarisation being more affected than the XX polarisation. Therefore, the worst affected area by RFI is located between 20 and 40 degrees North. However, a clear improvement of the situation is observed, mainly in Western Europe where the teams fighting against illegal sources of RFI have been most active. Static sources of RFI are still remaining, but they are of less intensity. Other areas with large variability, and not affected by RFI, are very interesting from an assimilation point of view. Snow covered areas clearly affect first-guess departures at the XX polarisation, because in these areas the CMEM modeled brightness temperatures are largely underestimated. A systematic negative bias is affecting the YY polarisation.
Over continental surfaces, the variability of the time series is dominated by the influence of the snow covered areas and RFI. The Southern Hemisphere presents more stable bias throughout the year, mainly because it is less affected by RFI and has a lower annual snow coverage. The bias are also very dependent on the incidence angle, as shown in the plots of the angular distribution of bias. In general, they increase with the incidence angle for XX polarisation, whereas they are maximum at 30 degrees for YY polarisation. While one of the objectives of the monitoring is to report on all types of land cover, it should be noted that snow covered areas will be masked in SMOS assimilation experiments, as the link to soil moisture is lost.

The current parameterisation of the ocean emission at L-band only accounts for the emission over a smooth surface of water. The effect of the wind and of the galactic noise is not currently accounted for. Thus, the results presented in this report over oceans are preliminary. Observed brightness temperatures and first-guess departures are much more homogeneous than for land pixels, as by nature oceans present less heterogeneities. The polar regions present a clear contrast compared to the rest of the oceans, as these regions are affected by sea ice and snow cover, or a mixture of frozen and liquid water, with very different dielectric properties and brightness temperatures.

The thermal stability test that took place in the end of December 2010 affected the NRT data until mid-February 2011. The degradation of the data in this period is clearly observed in the time series, but also in the geographical and Hovmöller maps. Using all these types of plots together, makes it possible to localize in time and space punctual problems in the data and/or the model.

Acknowledgements

This work is funded under the ESA-ESRIN contract number 4000101703/10/NL/FF/fk and is the second (MR2) of a series of Monitoring Reports to ESA. The authors would like to thank Ioannis Mallas at ECMWF, for the operational acquisition and contribution to the processing of the data. Also many thanks to Rob Hine and Anabel Bowen, both ECMWF, for their great help with the figures shown in this report.

6 References

References

[Balsamo et al. 2009] Balsamo, G., P. Viterbo, A. Beljaars, B. van den Hurk, M. Hirschi, A. Betts, and K. Scipal, 2009 : A revised hydrology for the ECMWF model: Verification from field site to terrestrial water storage and impact in the integrated forecast system. *Journal of Hydrometeorology*, **10**,623–643. doi: 10.1175/2008JHM1068.1.

[Choudhury et al. 1979] Choudhury, B. J., T. J. Schmugge, A. Chang, and R. W. Newton, 1979 : Effect of surface roughness on the microwave emission for soils. *Journal of Geophysical Research*, **84**,5699–5706.

[de Rosnay et al. 2009a] de Rosnay, P., M. Drusch, A. Boone, G. Balsamo, B. Decharme, P. Harris, Y. Kerr, T. Pellarin, J. Polcher, and J.-P. Wigneron, 2009a : AMMA Land Surface Model Intercomparison Experiment coupled to the Community Microwave Emission Model: ALMIP-MEM. *J. Geophys. Res.*, **114**. D05108, doi:10.1029/2008JD010724.

[de Rosnay et al. 2009b] de Rosnay, P., M. Drusch, and J.M. Sabater, 2009b : Milestone 1 Technical Note Part I: SMOS global surface emission model. Technical report, European Centre for Medium-Range Weather Forecast, Reading, United Kingdom.

[Drusch et al. 2001] Drusch, M., T. Holmes, P. de Rosnay, and G. Balsamo, 2001 : Vegetative and atmospheric corrections for the soil moisture retrieval from passive microwave remote sensing data: Results from the southern great plains hydrology experiment 1997. *J. Hydrometeor.*, **2**,181–192.

[Drusch et al. 2009] Drusch, M., T. Holmes, P. de Rosnay, and G. Balsamo, 2009 : Comparing ERA-40 based L-band brightness temperatures with Skylab observations: A calibration / validation study using the Community Microwave Emission Model. *J. Hydrometeor.*, **10**,213–226. doi: 10.1175/2008JHM964.1.

[Holmes et al. 2008] Holmes, T., M. Drusch, J.-P. Wigneron, and R. de Jeu, 2008 : A global simulation of microwave emission: Error structures based on output from ECMWFS operational integrated forecast system. *IEEE Transactions on Geoscience and Remote Sensing*, **46**,846 – 856.

[Kirdyashev et al. 1979] Kirdyashev, K., A. Chukhlantsev, and A. Shutko, 1979 : Microwave radiation of the earth's surface in the presence of vegetation cover. *Radiotekhnika i Elektronika*, **24**,256–264.

[Matos and Gutierrez 2004] Matos, P., and A. Gutierrez, 2004 : SMOS L1 processor discrete global grids document. Technical report, Deimos Engenharia, Lisboa, Portugal.

[Pellarin et al. 2003] Pellarin, T., J.-P. Wigneron, J.-C. Calvet, and P. Waldteufel, 2003 : Global soil moisture retrieval from a synthetic l-band brightness temperature data set. *Journal of Geophysical Research*, **108**.

[Sabater et al. 2011a] Sabater, J.M., P. de Rosnay, and G.Balsamo, 2011a : Sensitivity of L-band NWP forward modelling to soil roughness. *Int. J. Remote Sens.*, pp. 1–14. iFirst 2011., doi: 10.1080/01431161.2010.507260.

[Sabater et al. 2011b] Sabater, J.M., P. de Rosnay, and M. Dahoui, 2011b : SMOS Continuous Monitoring Reports; Part I. Technical report, European Centre for Medium-Range Weather Forecasts, Reading, United Kingdom.

[Sabater et al. 2010] Sabater, J.M., P. de Rosnay, and A. Fouilloux, 2010 : Milestone 2 Technical Note, Part I:operational pre-processing chain, Part II:collocation software development, Part III: Offline monitoring suite. Technical report, European Centre for Medium-Range Weather Forecasts, Reading, United Kingdom.

[Salgado 1999] Salgado, R., 1999 : Global soil maps of sand and clay fractions and of the soil depth for MESONH simulation based on FAO/UNESCO soil maps. Technical report, CNRM/Météo France. Tech. Note, **59**.

[Wang and Schmugge 1980] Wang, J. R., and T. Schmugge, 1980 : An empirical model for the complex dielectric permittivity of soils as a function of water content. *IEEE Transactions on Geoscience and Remote Sensing*, **18**,288–295.

[Wigneron et al. 2007] Wigneron, J.-P., Y. Kerr, P. Waldteufel, K. Saleh, M.-J. Escorihuela, P. Richaume, P. Ferrazzoli, P. de Rosnay, R. Gurneye, J.-C. Calvet, J. Grant, M. Guglielmetti, B. Hornbuckle, C. Mtzler, T. Pellarin, and M. Schwank, 2007 : L-band microwave emission of the biosphere (L-MEB) model: Description and calibration against experimental data sets over crop fields. *Remote Sensing of Environment*, **107**,639–655.

[Wigneron et al. 2001] Wigneron, J. P., L. Laguerre, and Y. Kerr, 2001 : A simple parameterization of the L-band microwave emission from rough agricultural soils. *IEEE Transactions on Geoscience and Remote Sensing*, **39**,1697–1707.